IEEE Photonics Journal
An IEEE Photonics Society Publication

Open Access

Design Rules for Raman Lasers Based on SOI Racetrack Resonators

Volume 5, Number 6, December 2013

F. De Leonardis
B. Troia
V. M. N. Passaro, Senior Member, IEEE

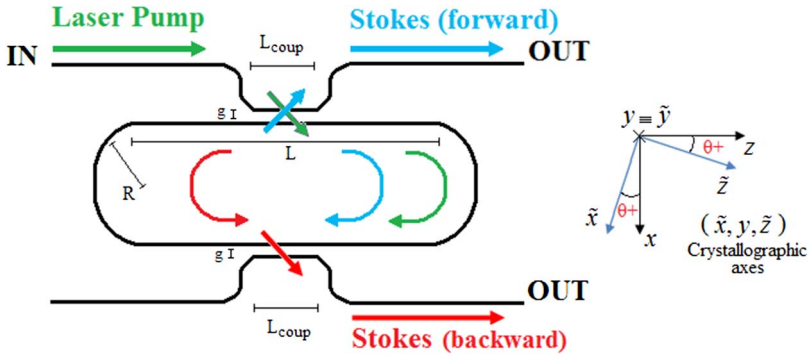

DOI: 10.1109/JPHOT.2013.2287562
1943-0655 © 2013 IEEE

IEEE photonics SOCIETY

IEEE

Design Rules for Raman Lasers Based on SOI Racetrack Resonators

F. De Leonardis, B. Troia, and V. M. N. Passaro, *Senior Member, IEEE*

Dipartimento di Ingegneria Elettrica e dell'Informazione, Politecnico di Bari, 70125 Bari, Italy

DOI: 10.1109/JPHOT.2013.2287562
1943-0655 © 2013 IEEE

Manuscript received September 3, 2013; revised October 8, 2013; accepted October 9, 2013. Date of publication October 28, 2013; date of current version November 4, 2013. This work was supported by the European Commission-Research Executive Agency through project FP7-SPACE-1-2012 "Modular CMOS Photonic Integrated Micro-Gyroscope" (MERMIG) under Grant 313037. Corresponding author: V. M. N. Passaro (e-mail: passaro@deemail.poliba.it).

Abstract: In this paper, the detailed modeling of Raman lasers in silicon-on-insulator guided-wave racetrack resonant microcavities is developed. Modeling based on full-vectorial equations and systematic design rules are presented for the first time. Simulation results are compared with experimental and theoretical results in literature, demonstrating a very good agreement. Moreover, parametric investigations including waveguide sizes, pump and Stokes coupling factors, cavity shape, polarization states, and waveguide orientation are presented, and their influence on the laser features are discussed.

Index Terms: Coherent sources modeling and theory, waveguide devices, nonlinear optical effects in semiconductors, silicon nanophotonics.

1. Introduction

In the last decade, an increasing interest has been widely devoted to silicon photonics [1]. In fact, silicon is considered as an ideal platform to overcome some actual limitations that the photonics industry still introduces with respect to Microelectronics [2], [3]. They can be summarized as follows: i) a variety of different materials used in photonics instead of one: InP as substrate for source development, silica as material for fibers, lithium niobate for modulators, other materials for dense wavelength-division-multiplexers (DWDM) and fiber amplifiers, to name a few; ii) no single material or single technology leading the market; iii) photonics industry characterized by many different small companies which are only specialized in specific devices. Moreover, chip scale integration of optical components, enabling low cost and mass-scale production, is not yet achieved. Nowadays, the development of silicon photonics involves some crucial areas of investigation, such as selective guiding and transporting of light within the silicon, encoding light, detecting light, amplification and generation of light, device packaging and, finally, intelligent control of all these photonic functionalities.

To this purpose, while a wide variety of passive devices were developed since the 1990s, recent activities have been focused on achieving active functionalities (mostly light amplification and generation) in silicon-on-insulator (SOI) waveguides. The need to develop very efficient silicon-based sources and integrated photonic circuits (PIC), in SOI technology platform, represents the current strategy employed by the industrial giants such as Intel, IBM, and Hewlett Packard in order to upgrade the microelectronic computing platform, whose intrinsic performances are almost saturated. To this purpose, optical interconnects on complementary metal-oxide semiconductor

(CMOS) chips constitute an important driver for silicon lasers, which can solve the communications bottleneck caused by the conventional metallic electrical interconnects. The main drawback of silicon, represented by its indirect bandgap and resulting in an extremely poor internal quantum efficiency for light emission, has been recently faced by investigating the integration of active III-V devices and passive silicon photonic components on the same SOI chip [4]–[6]. However, the large lattice and thermal mismatch between silicon and III-V material systems and alloys typically result in a large dislocation density, which limits the laser efficiency and reliability. On the other hand, silicon Raman lasers represent crucial devices in silicon photonics, to be employed as wavelength converters and amplifiers characterized by very high performance. However, they are not practical for interconnect applications since they need to be optically pumped by an external laser.

In this context, various approaches have been investigated based on silicon-engineered materials, including silicon nanocrystals [7]–[9], Er-doped silicon oxides [10], Si/SiGe structures [11], and porous silicon [12]. Recently, a different approach has been demonstrated, based on stimulated Raman scattering (SRS) effect [13]–[17]. It exploits the very high SRS gain coefficient in silicon guided-wave structures, being about four orders of magnitude larger than the silica one. Additionally, SOI waveguides allow to confine the optical field to an area that is approximately 100 times smaller than the modal area in a standard single-mode optical fiber, making SRS observable over the millimeter-scale interaction length, typical in integrated optical devices. Starting from 2002, several experimental and theoretical studies based on this effect have been proposed in literature, such as Raman amplification in SOI waveguides [18]–[23], Stokes and anti-Stokes Raman conversion [24]–[26], cross phase modulation (XPM)-based interferometer switch [27], two-photon absorption (TPA) [28], [29], and lossless modulation [30]. Moreover, the use of a resonant microcavity to enhance the Raman effect represents a strong stimulus toward the development of microscale Raman lasers with low threshold, as demonstrated in some pioneering works [31]–[33].

Recently, a detailed modeling of Raman amplification in SOI guided-wave resonant microcavities has been proposed in [34], demonstrating a very good agreement between theoretical and experimental results. In addition, the dependence of the Raman gain in silicon photonic waveguides on the substrate crystallographic axes, as well as the relative propagation directions of the pump and Stokes waves due to strong longitudinal mode-field components, has been demonstrated in several works [35]–[37] by using a full vectorial approach. More recently, a generic model has been introduced in [38] to describe the lasing characteristics of continuous-wave (CW) circular and racetrack-shaped ring Raman lasers based on micro- and nano-scale silicon waveguides.

Therefore, the contribution presented by this work is a systematic study to outline the fundamental design rules for Raman lasing effect in race-track SOI resonators, since the papers cited in literature only analyze the physical features of Raman laser for a well defined geometry and waveguide cross-section. On the contrary, the goal of this paper is to propose, starting from a general mathematical model, a number of parametric simulations to find the design guidelines for a race-track Raman laser, in order to predict both polarization state and directionality of its emission, laser threshold, and quantum external efficiency. Thus, the paper is organized as follows. In Section 2, we derive the mathematical model to study the Raman lasing in the race-track SOI resonators coupled to the external waveguides. The proposed modeling includes all nonlinear effects involved in the integrated structure without any a-priori assumption, i.e., SRS, TPA, free carrier absorption (FCA) induced by TPA, plasma dispersion effect, self-phase-modulation (SPM), and XPM effects, as induced by Kerr nonlinearity. In addition, the model takes into account the polarization effect, the emission directionality of the Stokes waves, the mismatch between the input beam wavelengths and the microcavity resonance wavelengths, as well as the coupling mechanism between the microcavity and input/output bus waveguides. In Section 3, a number of numerical results are shown, including comparisons between our theory and some experiments presented in literature on CW Raman lasers based on racetrack resonators. Moreover, a parametric study to select the fundamental design rules for Raman excitation in SOI race-track microcavity is carried out. Performances in terms of power emission, threshold level, and external efficiency are evaluated for two different SOI cross-sectional waveguides. Finally, Section 4 summarizes the conclusions.

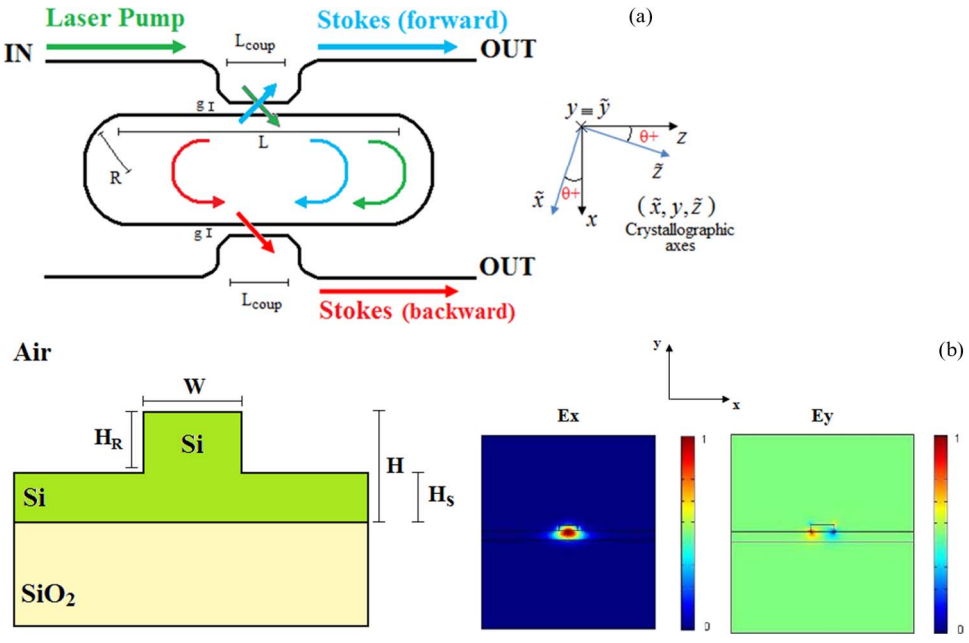

Fig. 1. (a) Schematic architecture of a SOI race-track resonator coupled to the external waveguides. (b) SOI waveguide cross-section with E_x-Field and E_y-Field spatial distributions of the quasi-TE polarized optical mode at $\lambda = 1.55$ μm ($W = 700$ nm, $H = 500$ nm, $H_S = 300$ nm, $H_R = 200$ nm).

2. Modeling

2.1. General Model

In this section, we propose, according to the full vectorial approach presented in [35]–[37], the general physical model for the analysis of nonlinear effects occurring in a race-track resonator based on SOI technology. The proposed model is based on a set of partial differential equations for the nonlinear coupling between pump and fundamental Stokes waves inside the microcavity, and one rate equation for the hole-electron pairs generated in the resonator by the TPA effect, as induced by pump and Stokes waves.

In our analysis, we assume the architecture as sketched in Fig. 1(a), where the input pump (S_p) is injected in the resonator by means of the evanescent coupling between the resonant microcavity and the input external bus, both based on rib waveguides in SOI, where g and L_{coup} are the directional coupler gap and length, respectively. Moreover, an additional bus has been also considered, although it is not needed in principle for the analysis of the laser physical behavior. In most of the photonic applications and experimental devices, for improving the Raman gain, the microcavity is a racetrack resonator as in Fig. 1(a), as it will be more clear in the following.

In Fig. 1(b), the waveguide cross-section is sketched, showing also the E_x-field and E_y-field spatial distributions of the quasi transverse electric (i.e., quasi-TE) polarized optical mode at the operative wavelength $\lambda = 1.55$ μm, as well as the main geometrical parameters, including the rib etch depth H_R and width W, the overall waveguide height H, and the slab height H_S. Numerical simulations have been performed by using a full-vectorial finite-element method (FEM) [39], with a total domain area of about 12 μm^2 and approximately 90 000 triangular mesh elements. The same waveguide cross-section has been always assumed for input and output buses, directional couplers, and race-track resonator. Furthermore, in the proposed design procedure, silicon waveguide geometrical dimensions are considered as variable parameters, to be optimized for the excitation of Stokes signals inside the SOI racetrack resonator, according to design rules that will be presented in this work.

Without any lack of generality, we assume that the electric field inside the microcavity is predominantly a single transverse mode. This condition is appropriately satisfied by choosing rib waveguide sizes in order to meet the single-mode condition. Thus, up to two propagating modes can be assumed as confined in the resonator, one quasi-TE (dominant horizontal x-component of electric field) and one quasi-TM (dominant vertical y-component of electric field), where x and y designate the waveguide cross section coordinates.

Hereinafter, the input pump wave (S_p) is aligned with quasi-TE or quasi-TM polarization. In addition, by neglecting the polarization cross-coupling between waveguide and resonator (condition usually satisfied in SOI directional couplers), the pump wave inside the resonant cavity is assumed to hold the same polarizations as S_p, thus inducing Stokes waves aligned with quasi-TE or quasi-TM modes (depending on the laser features).

We indicate with $\mathbf{e}_p$, $\mathbf{e}_{s+}$, and $\mathbf{e}_{s-}$ the electric field vectors of the pump (p) and Stokes (s) modes, respectively, with real transverse and imaginary longitudinal components. In particular, $\mathbf{e}_{s+}$ represents the Stokes wave co-propagating with the pump inside the resonator. Moreover, $\mathbf{e}_{s-}$ indicates the counter-propagating Stokes mode which, for definition, has the same transverse components as $\mathbf{e}_{s+}$ but with the longitudinal component equal to the complex conjugate. Finally, the electric field $\mathbf{e}_{p,s\pm}$ is normalized by means of the following coefficient:

$$\hat{N}_i = \frac{1}{2}\int \left[\mathbf{e}_i(x,y) \times \mathbf{h}_i^*(x,y)\right] \cdot \hat{z}\, dx\, dy \qquad \text{with} \quad i = p, s+, s- \tag{1}$$

In Eq. (1), we have assumed the electro-magnetic field evaluated in the waveguide coordinate system (x, y, z), generally rotated by an angle θ with respect to the crystallographic axes $(\tilde{x}, \tilde{y}, \tilde{z})$. Thus, the mode fields are given by means of the rotation matrix in the form

$$\begin{pmatrix} e_i^{\tilde{x}} \\ e_i^{\tilde{y}} \\ e_i^{\tilde{z}} \end{pmatrix} = \begin{pmatrix} \cos(\theta) & 0 & -\sin(\theta) \\ 0 & 1 & 0 \\ \sin(\theta) & 0 & \cos(\theta) \end{pmatrix} \begin{pmatrix} e_i^{x} \\ e_i^{y} \\ e_i^{z} \end{pmatrix}. \tag{2}$$

Consequently, the electric field inside the race-track resonator can be written as

$$\mathbf{e}(x,y,z,t) = \left[\sum_n \mathbf{e}_{p,n} e^{j(\beta_{p,n} z - \omega_{p,n} t)} + c.c.\right] + \left[\sum_l \mathbf{e}_{s,l} e^{j(\beta_{s,l} z - \omega_{s,l} t)} + c.c.\right] \tag{3}$$

where c.c. indicates the conjugate complex terms; the subscripts n and l designate all possible longitudinal resonant modes in the cavity for pump and Stokes waves, respectively; $\omega_{p,n}$ $(\omega_{s,l})$ is the resonant angular pulsation of pump (Stokes) mode inside the cavity; and $\beta_{p,n}$ $(\beta_{s,l})$ is the propagation constant of pump (Stokes) wave under the resonance condition.

It is clear that, if the resonator is excited from an external optical beam travelling in the bus waveguide, only a few terms have to be considered in the summations of Eq. (3). In fact, if the input pump (S_p) is launched into the bus waveguide with an angular frequency ω_p, the generated Stokes wave will have an angular frequency ω_s, where $\omega_p - \omega_s = \Omega_R$, and $\Omega_R = 15.6$ THz is the Raman frequency shift in silicon. Then, only those resonant modes whose angular frequencies are closer to ω_p and ω_s will give a contribution to summations in Eq. (3). These modes are characterized by longitudinal orders, i.e., $\bar{n}$ and $\bar{l}$, according to the resonance condition as $\bar{n} \sim (\omega_p n_{eff,p} L_{cavity})/(2\pi c)$ and $\bar{l} \sim (\omega_s n_{eff,s} L_{cavity})/(2\pi c)$, where L_{cavity} is the cavity length, $n_{eff,p}$ $(n_{eff,s})$ is the effective index of pump (Stokes) wave inside the ring resonator, and c is the light velocity in vacuum.

The presence of only two resonant modes in the microcavity holds if the cavity free spectral range (FSR) is larger than the input pulse bandwidth, $\Delta\omega_{pulse}$. For example, by assuming a Gaussian input pump pulse with full-width-at-half-maximum (FWHM) time width T_{FWHM}, the condition $FSR > \Delta\omega_{pulse}$ means $L_{cavity} < (2\pi c T_{FWHM})/(2\sqrt{2\ln 2} n_{eff,p})$.

According to the full-vectorial nonlinear coupled mode theory (CMT), the equations describing the power transfer among the pump wave (p) and fundamental Stokes waves (s) can be written as

$$\begin{aligned}\frac{\partial a_p}{\partial t}+v_{g,p}\frac{\partial a_p}{\partial z}=&j(\omega_{p,\bar{n}}-\omega_p)a_p-\frac{1}{2}\frac{1}{\tau_p}a_p-\frac{1}{2}v_{g,p}\alpha_p^{(FCA)}a_p\\&-v_{g,p}\left[\frac{1}{2}\frac{\beta_{pp}^{TPA}}{A_{p,p}^{TPA}}|a_p|^2+\frac{\beta_{ps+}^{TPA}}{A_{p+,s+TE}^{TPA}}|a_{s+TE}|^2+\frac{\beta_{ps-}^{TPA}}{A_{p+,s-TE}^{TPA}}|a_{s-TE}|^2\right.\\&\left.+\frac{\beta_{ps+}^{TPA}}{A_{p,s+TM}^{TPA}}|a_{s+TM}|^2+\frac{\beta_{ps-}^{TPA}}{A_{p,s-TM}^{TPA}}|a_{s-TM}|^2\right]a_p\\&-v_{g,p}\left[\frac{1}{2}\frac{\lambda_s}{\lambda_p}g_{s+,TE}^{eff}|a_{s+TE}|^2+\frac{1}{2}\frac{\lambda_s}{\lambda_p}g_{s-,TE}^{eff}|a_{s-TE}|^2\right.\\&\left.+\frac{1}{2}\frac{\lambda_s}{\lambda_p}g_{s+,TM}^{eff}|a_{s+TM}|^2+\frac{1}{2}\frac{\lambda_s}{\lambda_p}g_{s-,TM}^{eff}|a_{s-TM}|^2\right]a_p\\&+jv_{g,p}\left[\frac{\gamma_p}{A_{p,p}^{Kerr}}|a_p|^2+2\frac{\gamma_p}{A_{p,s+TE}^{Kerr}}|a_{s+TE}|^2+2\frac{\gamma_p}{A_{p,s-TE}^{Kerr}}|a_{s-TE}|^2\right.\\&\left.+2\frac{\gamma_p}{A_{p,s+TM}^{Kerr}}|a_{s+TM}|^2+2\frac{\gamma_p}{A_{p,s-TM}^{Kerr}}|a_{s-TM}|^2\right]a_p+jv_{g,p}\frac{2\pi}{\lambda_p}\Delta n_p a_p+\xi_p S_p\end{aligned}\tag{4}$$

$$\begin{aligned}\frac{\partial a_{s+TE}}{\partial t}+v_{g,s}\frac{\partial a_{s+TE}}{\partial z}=&j(\omega_{s,\bar{l}}-\omega_s)a_{s+TE}-\frac{1}{2}\frac{1}{\tau_s}a_{s+TE}-\frac{1}{2}v_{g,s}\alpha_s^{(FCA)}a_{s+TE}+v_{g,s}\left[\frac{1}{2}g_{s+,TE}^{eff}|a_p|^2\right]a_{s+TE}\\&-v_{g,s}\left[\frac{1}{2}\frac{\beta_{s+s+}^{TPA}}{A_{s+TE,s+TE}^{TPA}}|a_{s+TE}|^2+\frac{\beta_{s+p+}^{TPA}}{A_{s+TE,p}^{TPA}}|a_p|^2+\frac{\beta_{s+s-}^{TPA}}{A_{s+TE,s-TE}^{TPA}}|a_{s-TE}|^2\right.\\&\left.+\frac{\beta_{s+s-}^{TPA}}{A_{s+TE,s+TM}^{TPA}}|a_{s+TM}|^2+\frac{\beta_{s+s-}^{TPA}}{A_{s+TE,s-TM}^{TPA}}|a_{s-TM}|^2\right]a_{s+TE}\\&+jv_{g,s}\left[\frac{\gamma_s}{A_{s+TE,s+TE}^{Kerr}}|a_{s+TE}|^2+2\frac{\gamma_s}{A_{s+TE,p}^{Kerr}}|a_p|^2+2\frac{\gamma_s}{A_{s+TE,s-TE}^{Kerr}}|a_{s-TE}|^2\right.\\&\left.+2\frac{\gamma_s}{A_{s+TE,s+TM}^{Kerr}}|a_{s+TM}|^2+2\frac{\gamma_s}{A_{s+TE,s-TM}^{Kerr}}|a_{s-TM}|^2\right]a_{s+TE}\\&+jv_{g,s}\frac{2\pi}{\lambda_s}\Delta n_s a_{s+TE}-\frac{1}{2}b_{s+}a_{s-TE}-\frac{1}{2}b_{s+}a_{s-TM}\end{aligned}\tag{5}$$

$$\begin{aligned}\frac{\partial a_{s-TE}}{\partial t}-v_{g,s}\frac{\partial a_{s-TE}}{\partial z}=&j(\omega_{s,\bar{l}}-\omega_s)a_{s-TE}-\frac{1}{2}\frac{1}{\tau_s}a_{s-TE}-\frac{1}{2}v_{g,s}\alpha_s^{(FCA)}a_{s-TE}+v_{g,s}\left[\frac{1}{2}g_{s-,TE}^{eff}|a_p|^2\right]a_{s-TE}\\&-v_{g,s-}\left[\frac{1}{2}\frac{\beta_{s-s-}^{TPA}}{A_{s-TE,s-TE}^{TPA}}|a_{s-TE}|^2+\frac{\beta_{s-p}^{TPA}}{A_{s-TE,p}^{TPA}}|a_p|^2+\frac{\beta_{s-s+}^{TPA}}{A_{s-TE,s+TE}^{TPA}}|a_{s+TE}|^2\right.\\&\left.+\frac{\beta_{s-s+}^{TPA}}{A_{s-TE,s+TM}^{TPA}}|a_{s+TM}|^2+\frac{\beta_{s-s-}^{TPA}}{A_{s-TE,s-TM}^{TPA}}|a_{s-TM}|^2\right]a_{s-TE}\\&+jv_{g,s}\left[\frac{\gamma_s}{A_{s-TE,s-TE}^{Kerr}}|a_{s-TE}|^2+2\frac{\gamma_s}{A_{s-TE,p}^{Kerr}}|a_p|^2+2\frac{\gamma_s}{A_{s-TE,s+TE}^{Kerr}}|a_{s+TE}|^2\right.\\&\left.+2\frac{\gamma_s}{A_{s-TE,s+TM}^{Kerr}}|a_{s+TM}|^2+2\frac{\gamma_s}{A_{s-TE,s-TM}^{Kerr}}|a_{s-TM}|^2\right]a_{s-TE}\\&+jv_{g,s}\frac{2\pi}{\lambda_s}\Delta n_s a_{s-TE}-\frac{1}{2}b_{s-}a_{s+TE}-\frac{1}{2}b_{s-}a_{s+TM}\end{aligned}\tag{6}$$

$$\begin{aligned}
&\frac{\partial a_{s+TM}}{\partial t} + v_{g,s}\frac{\partial a_{s+TM}}{\partial z} \\
&= j(\omega_{s,\bar{l}} - \omega_s)a_{s+TM} - \frac{1}{2}\frac{1}{\tau_s}a_{s+TM} - \frac{1}{2}v_{g,s}\alpha_s^{(FCA)}a_{s+TM} + v_{g,s}\left[\frac{1}{2}g_{s+,TM}^{eff}|a_p|^2\right]a_{s+TM} \\
&\quad - v_{g,s}\left[\frac{1}{2}\frac{\beta_{s+s+}^{TPA}}{A_{s+TM,s+TM}^{TPA}}|a_{s+TM}|^2 + \frac{\beta_{s+p}^{TPA}}{A_{s+TM,p}^{TPA}}|a_p|^2 + \frac{\beta_{s+s-}^{TPA}}{A_{s+TM,s+TE}^{TPA}}|a_{s+TE}|^2\right. \\
&\qquad \left. + \frac{\beta_{s+s-}^{TPA}}{A_{s+TM,s-TE}^{TPA}}|a_{s-TE}|^2 + \frac{\beta_{s+s-}^{TPA}}{A_{s+TM,s-TM}^{TPA}}|a_{s-TM}|^2\right]a_{s+TM} \\
&\quad + jv_{g,s}\left[\frac{\gamma_s}{A_{s+TM,s+TM}^{Kerr}}|a_{s+TM}|^2 + 2\frac{\gamma_s}{A_{s+TM,p}^{Kerr}}|a_p|^2 + 2\frac{\gamma_s}{A_{s+TM,s+TE}^{Kerr}}|a_{s+TE}|^2\right. \\
&\qquad \left. + 2\frac{\gamma_s}{A_{s+TM,s-TE}^{Kerr}}|a_{s-TE}|^2 + 2\frac{\gamma_s}{A_{s+TM,s-TM}^{Kerr}}|a_{s-TM}|^2\right]a_{s+TM} \\
&\quad + jv_{g,s}\frac{2\pi}{\lambda_s}\Delta n_s a_{s+TM} - \frac{1}{2}b_{s+}a_{s-TE} - \frac{1}{2}b_{s+}a_{s-TM}
\end{aligned} \tag{7}$$

$$\begin{aligned}
&\frac{\partial a_{s-TM}}{\partial t} - v_{g,s}\frac{\partial a_{s-TM}}{\partial z} \\
&= j(\omega_{s,\bar{l}} - \omega_{s-})a_{s-TM} - \frac{1}{2}\frac{1}{\tau_s}a_{s-TM} - \frac{1}{2}v_{g,s}\alpha_s^{(FCA)}a_{s-TM} + v_{g,s}\left[\frac{1}{2}g_{s-,TM}^{eff}|a_p|^2\right]a_{s-TM} \\
&\quad - v_{g,s}\left[\frac{1}{2}\frac{\beta_{s-s-}^{TPA}}{A_{s-TM,s-TM}^{TPA}}|a_{s-TM}|^2 + \frac{\beta_{s-p}^{TPA}}{A_{s-TM,p}^{TPA}}|a_p|^2 + \frac{\beta_{s-s+}^{TPA}}{A_{s-TM,s+TE}^{TPA}}|a_{s+TE}|^2\right. \\
&\qquad \left. + \frac{\beta_{s-s+}^{TPA}}{A_{s-TM,s-TE}^{TPA}}|a_{s-TE}|^2 + \frac{\beta_{s-s-}^{TPA}}{A_{s-TM,s+TM}^{TPA}}|a_{s+TM}|^2\right]a_{s-TM} \\
&\quad + jv_{g,s}\left[\frac{\gamma_s}{A_{s-TM,s-TM}^{Kerr}}|a_{s-TM}|^2 + 2\frac{\gamma_s}{A_{s-TM,p}^{Kerr}}|a_p|^2 + 2\frac{\gamma_s}{A_{s-TM,s+TE}^{Kerr}}|a_{s+TE}|^2\right. \\
&\qquad \left. + 2\frac{\gamma_s}{A_{s-TM,s-TE}^{Kerr}}|a_{s-TE}|^2 + 2\frac{\gamma_s}{A_{s-TM,s+TM}^{Kerr}}|a_{s+TM}|^2\right]a_{s-TM} \\
&\quad + jv_{g,s}\frac{2\pi}{\lambda_s}\Delta n_s a_{s-TM} - \frac{1}{2}b_{s-}a_{s+TE} - \frac{1}{2}b_{s-}a_{s+TM}
\end{aligned} \tag{8}$$

where a_p, $a_{s\rho\sigma}$ represent the slowly varying field amplitudes (time, z functions) for the pump and Stokes waves inside the race-track resonator, respectively, with $\rho = +, -$ and $\sigma =$ TE, TM. Thus, the system of Eqs. (4)–(8) is complete taking into account the possible excitation of Stokes waves in both propagation directions with respect to the pump as well as both states of polarization (quasi-TE and quasi-TM). Group velocity dispersion (GVD) is not included as second order time derivative, since this effect is negligible in SOI micro-scale structures [40] and for $T_{FWHM} > 1$ ps (as in most of the laser applications). Moreover, the power transferred to higher order Stokes waves is also negligible for short interaction lengths and relatively large values of T_{FWHM}, as in this work.

The terms $(\omega_{p,\bar{n}} - \omega_p)$ and $(\omega_{s,\bar{l}} - \omega_s)$ indicate the mismatch from the resonance condition of input pump and Stokes waves frequency, respectively. The term τ_p (τ_s) represents the overall photon decay time of the pump (Stokes) wave inside the cavity. It is related to the overall resonator quality factor by means of the relationship $Q_p = \omega_p\tau_p$, where τ_p is given by

$$\frac{1}{\tau_p} = \frac{1}{\tau_p^I} + \frac{1}{\tau_p^{c,1}} + \frac{1}{\tau_p^{c,2}} \tag{9}$$

being the three contributions related to loss (τ_p^I), input bus coupling $(\tau_p^{c,1})$, and output bus coupling $(\tau_p^{c,2})$, and time constants. Similar definition holds for τ_s. Furthermore, the decay time related to

losses can be also given as a function of the overall linear loss coefficient (α_{loss}) by means of the relationship $\tau_i^l = 1/(\alpha_{loss,i} v_{g,i})$, where $v_{g,i}$ is the wave group velocity $(i = p, s+, s-)$. Moreover, coefficient ξ_p in Eq. (4) is related to the power fraction transferred into the resonator from the input pump (S_p) as follows: $\xi_p = \sqrt{(v_{g,p}/L_{cavity})(1/\tau_p^{c,1})}$. Hereinafter, it is convenient to introduce the coupling factor $\kappa_{p,j}^2$ $(\kappa_{s,j}^2)$, defined as the power fraction of the input pump (Stokes) wave coupled between the race-track resonator and the external bus waveguides. It is possible to demonstrate that the coupling factor $\kappa_{p,j}^2$ $(\kappa_{s,j}^2)$ is related to the coupling time constant $\tau_p^{c,j}$ $(\tau_s^{c,j})$, $j = 1, 2$ by means of the following equations [40]:

$$\kappa_{p,j}^2 = \frac{1}{\tau_p^{c,j}} \frac{L_{cavity}}{v_{g,p}} \tag{10.a}$$

$$\kappa_{s,j}^2 = \frac{1}{\tau_s^{c,j}} \frac{L_{cavity}}{v_{g,s}}. \tag{10.b}$$

Furthermore, in Eqs. (4)–(8), the terms with $\beta_{ij}^{(TPA)}$ $(i = p, s+, s-)$ represent the TPA effect on the ith beam induced by the jth wave. Moreover, the coefficients $\gamma_i = n_2 \omega_i / c$ take into account the SPM and XPM effects, as induced by Kerr nonlinearity, where n_2 is the nonlinear refractive index and ω_i the angular frequency of the ith beam inside the cavity.

The effective modal area relevant to the ith wave $(i = p, s+, s-)$ plays a fundamental role since it determines the efficiency with which any nonlinear effect manifests inside the optical SOI waveguide. According to the full vectorial CMT [35]–[37], the effective modal areas are calculated as

$$A_{s\rho\sigma,p}^{SRS} = \frac{4\mu_0 (\hat{N}_{s\rho\sigma} \hat{N}_p)}{\varepsilon_0 n_s n_p} \times \left\{ \iint \left[|\mathbf{e}_{s\rho\sigma}|^2 |\mathbf{e}_p|^2 + |\mathbf{e}_{s\rho\sigma} \cdot \mathbf{e}_p|^2 - 2\left(|\tilde{e}_{s\rho\sigma}^x|^2 |\tilde{e}_p^x|^2 + |\tilde{e}_{s\rho\sigma}^y|^2 |\tilde{e}_p^y|^2 + |\tilde{e}_{s\rho\sigma}^z|^2 |\tilde{e}_p^z|^2 \right) \right] dxdy \right\}^{-1} \tag{11}$$

$$A_{i,j}^{TPA} = A_{i,j}^{Kerr} = \frac{4\mu_0 (\hat{N}_i \hat{N}_j)}{\varepsilon_0 n_i n_j} \left[\frac{1}{3} \iint \left(|\mathbf{e}_i|^2 |\mathbf{e}_j|^2 + \left| \mathbf{e}_i \cdot (\mathbf{e}_j)^* \right|^2 + |\mathbf{e}_i \cdot \mathbf{e}_j|^2 \right) dxdy \right]^{-1} \quad (i, j = p, s_{+TE}, s_{-TE}, s_{+TM}, s_{-TM}) \tag{12}$$

where n_p, n_s is the refractive index at the pump and Stokes wavelengths, respectively, calculated through Sellmeier equations. Finally, $g_{s\rho,\sigma}^{eff}$ (with $\rho = +, -$ and $\sigma =$ TE, TM) represents the effective Raman gain into the race-track resonator for the Stokes wave with polarization state and propagation direction with respect to the pump, indicated by the indexes σ and ρ, respectively. It is defined as a microcavity average gain as follows:

$$g_{s\rho,\sigma}^{eff} = \frac{2L g_{s\rho}^{\sigma}\Big|_{\theta_0} + 2R \int_{\theta_0}^{\pi+\theta_0} g_{s\rho}^{\sigma}(\theta) d\theta}{2L + 2\pi R} \tag{13}$$

where θ_0 is the orientation of race-track straight section with respect to the crystallographic axes. In Eq. (13), the coefficient $g_{s\rho}^{\sigma}(\theta)$ depends on the Raman gain for bulk silicon and SRS effective modal area, as follows:

$$g_{s\rho}^{\sigma}(\theta) = \frac{g_{bulk}^{SRS}}{A_{s\rho\sigma,p}^{SRS}}. \tag{14}$$

By using the definition of SRS effective modal area in Eq. (11) and after some algebra, we obtain

$$g^{\sigma}_{s\rho}(\theta) = B^{\sigma}_{s\rho} - C^{\sigma}_{s\rho} - D^{\sigma}_{s\rho}[\cos(4\theta) + 3] - E^{\sigma}_{s\rho}[1 - \cos(4\theta)] \tag{15}$$

where

$$B^{\sigma}_{s\rho} = g^{SRS}_{bulk} \frac{\varepsilon_0 n_s n_p}{4\mu_0 \left(\hat{N}^{\sigma}_{s\rho}\hat{N}_p\right)} \left(\int\int \left[\left|\mathbf{e}^{\sigma}_{s\rho}\right|^2 |\mathbf{e}_p|^2 + \left|\mathbf{e}^{\sigma}_{s\rho} \cdot \mathbf{e}_p\right|^2 \right] dxdy \right)$$

$$C^{\sigma}_{s\rho} = g^{SRS}_{bulk} \frac{\varepsilon_0 n_s n_p}{4\mu_0 \left(\hat{N}^{\sigma}_{s\rho}\hat{N}_p\right)} \left(\int\int 2\left|\tilde{e}^{\sigma,y}_{s\rho}\right|^2 \left|\tilde{e}^{y}_{p}\right|^2 dxdy \right)$$

$$D^{\sigma}_{s\rho} = g^{SRS}_{bulk} \frac{\varepsilon_0 n_s n_p}{4\mu_0 \left(\hat{N}^{\sigma}_{s\rho}\hat{N}_p\right)} \left(\int\int \frac{1}{2}\left[\left(e^{\sigma,x}_{s\rho}\right)^2 \left(e^{x}_{p}\right)^2 + \left(\mathrm{Im}\left(e^{\sigma,z}_{s\rho}\right)\right)^2 \left(\mathrm{Im}\left(e^{z}_{p}\right)\right)^2 \right] dxdy \right)$$

$$E^{\sigma}_{s\rho} = g^{SRS}_{bulk} \frac{\varepsilon_0 n_s n_p}{4\mu_0 \left(\hat{N}^{\sigma}_{s\rho}\hat{N}_p\right)} \left(\int\int \frac{1}{2}\left[\left(e^{\sigma,x}_{s\rho}\right)^2 \left(\mathrm{Im}\left(e^{z}_{p}\right)\right)^2 + \left(\mathrm{Im}\left(e^{\sigma,z}_{s\rho}\right)\right)^2 \left(e^{x}_{p}\right)^2 \right] dxdy \right).$$

By substituting Eqs. (14) and (15) in (13) and solving the integral, we obtain the following relationship for the effective Raman gain:

$$g^{eff}_{s_{\rho,\sigma}} = \frac{g^{\sigma}_{s\rho}\Big|_{\theta_0} + R_{shape} g^{\sigma}_{s\rho}\Big|_{\theta=\pi/8}}{1 + R_{shape}} \tag{16}$$

where $R_{shape} = \pi R/L$ is the shape factor of the race-track resonator. Some comments can be derived from Eqs. (11)–(12), (14), and (16). First, the definition proposed in this paper in Eq. (11) for the effective Raman gain inside the race-track resonator allows a rigorous evaluation of the cavity shape influence on the Raman emission to be made. In addition, according to [35]–[38], Eqs. (11) and (14) take into account the polarization state and the silicon waveguide orientation with respect to the crystallographic axes.

Moreover, in Eqs. (4)–(8), $\alpha_i^{(FCA)}$, $i = p, s$, is the contribution to the total losses due to FCA, as induced by the change of free carrier density generated mainly by TPA of pump and Stokes waves. We have evaluated $\alpha_i^{(FCA)}$ according to Soref's relationship [41] as

$$\alpha_i^{(FCA)} = 8.5 \cdot 10^{-18} \times \left(\frac{\lambda_i}{1.55}\right)^2 \Delta N_e + 6.0 \cdot 10^{-18} \times \left(\frac{\lambda_i}{1.55}\right)^2 \Delta N_h = \sigma_i \times N_c = \sigma_0 \times \left(\frac{\lambda_i}{1.55}\right)^2 N_c$$

where $N_c = \Delta N_e = \Delta N_h$ is the density of electron-hole pairs generated by TPA process. The coefficient $\sigma_0 = 1.45 \cdot 10^{-17}$ cm^{-2} [24] is the FCA cross section measured at $\lambda = 1.55$ μm, and λ_i is the relevant mode (pump or Stokes wave) wavelength.

Furthermore, $\Delta n = -8.8 \cdot 10^{-22} \times (\lambda_i/1.55)^2 \times \Delta N_e - 8.5 \cdot 10^{-18} \times (\lambda_i/1.55)^2 \times (\Delta N_h)^{0.8} \approx -1.66 \times \delta_i \times N_c$ [41] is the change of effective index due to plasma dispersion effect, as induced by free carriers, where $\delta_i = 8.8 \cdot 10^{-22}(\lambda_i/1.55)^2$ [24]. The terms b_s represent the backscattering induced by the lateral roughness and depend on the amplitude reflectivity coefficient R_{back} ($|b_s| = (2cR_{back}/(n_{eff,s}L_{cavity}))$).

Finally, the full physical consistence of the system of Eqs. (4)–(8) requires the rate equation governing the free carrier dynamics into the waveguide core. Thus, generalizing the equation given in [20], we can write

$$\frac{dN_c}{dt} = -\frac{N_c}{\tau_{eff}} + \frac{1}{2}\sum_i \frac{\beta_{ii}^{(TPA)}}{\hbar\omega_i \left(A_{i,i}^{(TPA)}\right)^2}\left(P_i^2\right) + \frac{1}{2}\sum_i \sum_{j\neq i} \left(\frac{\beta_{ji}^{TPA}}{\hbar\omega_s \left(A_{j,i}^{TPA}\right)\left(A_{j,j}^{TPA}\right)} P_i P_j + \frac{\beta_{ji}^{TPA}}{\hbar\omega_s \left(A_{j,i}^{TPA}\right)\left(A_{i,i}^{(TPA)}\right)} P_i P_j \right)$$
$$i, j = p, s+TE, s-TE, s+TM, s-TM \tag{17}$$

where τ_{eff} is the effective recombination lifetime for free carriers, and $\hbar$ is the reduced Planck constant.

It seems interesting to outline some features in the mathematical model presented in this section, as well as in works proposed in literature. First, our model is based on a full-vectorial generalization of that proposed in [34] which, on the contrary, does not allow the influence of waveguide orientation and structure on the Raman gain to be appropriately taken into account. In addition, even though we propose a general formalism based on the full vectorial CMT as in [35]–[38], some important differences are not trivial. In fact, we include in the model the terms $(\omega_{p,\bar{n}} - \omega_p)$ and $(\omega_{s,\bar{l}} - \omega_s)$, indicating the mismatch from the resonance condition of input pump and Stokes waves frequency, respectively. It is intuitive to guess that the shorter the cavity length, the stronger the influence of such a mismatch. Consequently, it can be considered a critical factor for inducing Raman lasing in very small resonators with very high enhancement factors $(\Gamma = |a_p/S_p|)$. Moreover, in our model, the backscattering between Stokes waves is appropriately included, as due to the lateral roughness of the race-track resonator. This effect becomes very important in the possible applications of Raman laser for optical gyros, since it determines the width of the dead band region [42]. Finally, the general formalism proposed in this paper takes into account the walk-off effect (i.e., first order time derivative) between pump and Stokes waves inside the resonator. Thus, Raman lasers based on race-track SOI resonators can be analyzed in both pulsed and continuous wave regimes. However, in CW regime, our equations become similar to those in Ref. [38], except for the resonance mismatch and backscattering effect. It is worth to outline that, in the mathematical model, the stimulated Brillouin scattering (SBS) [43] has been neglected. In fact, although nano-scale modal confinement is known to radically enhance the effect of intrinsic Kerr and Raman nonlinearities within nanophotonic silicon waveguides, SBS effect is stifled in conventional silicon nanophotonics, requiring coherent coupling between guided photon and phonon modes. Recently, travelling-wave Brillouin non-linearities and Brillouin gain in silicon waveguides have been demonstrated through a novel class of hybrid photonic–phononic waveguides based on silicon waveguide core within the silicon nitride membrane [43].

Finally, additional comments are needed about cascaded Raman effect. The possibility to induce the cascaded Raman effect in SOI racetrack resonators has been already demonstrated [44] to further extend the laser emission in mid-infrared wavelength region. To this aim, directional couplers are to be designed under critical coupling condition for the pump wavelength and close to zero coupling condition for the first Stokes wavelength (thus achieving high intracavity power that generates Raman gain at the second-order Stokes wavelength) as well as low coupling for the second-order Stokes, in order to obtain at the same time both low lasing threshold and enough output power extraction from the resonator. However, design rules in this paper are completely different, because the aim is to optimize both threshold and quantum efficiency for the first order Stokes emission. Then, critical coupling is not satisfied and higher order Stokes waves in the partial differential equations system can be neglected in the most cases. In any case, the general model presented in this section could be easily extended to include further Stokes contributes, according to our previous work [45].

2.2. CW Laser Operation

In several applications, it is important to use the SRS for CW laser operation. From the system of Eqs. (4)–(8) and (17), we can observe that a quasi-CW regime occurs if the input pump time width T_{FWHM} in the bus waveguide satisfies the condition $T_{FWHM} \gg \max(\tau_p, \tau_{eff})$. Since τ_p is of the order of a few tens of picoseconds in the most cases, it must be $T_{FWHM} \geq 100$ ps, resulting in τ_{eff} as the dominant factor for the quasi-CW regime. Moreover, a large T_{FWHM} means that the group-velocity mismatch does not influence the SRS process in microcavities. Then, we can assume that the pump and the Stokes waves travel with the same velocity inside the resonator, and thus, the partial differential equations (4)–(8) can be transformed in ordinary differential equations by writing [46]

$$\frac{da_{p,s}}{dt} = \frac{\partial a_{p,s}}{\partial t} \pm v_g \frac{\partial a_{p,s}}{\partial z} \qquad \text{with} \quad v_{g,p} \cong v_{g,s} = v_g. \tag{18}$$

In this subsection, the relationship to calculate the threshold condition for the Raman lasing effect in the resonator under quasi-CW regime is found in closed form. A number of considerations can be made on the system of Eqs. (4)–(8) and (17) under assumption of Eq. (18). Quasi-CW regime means a steady-state analysis, where the threshold condition for SRS effect leads to neglect the terms depending on Kerr effect. In particular, SPM and XPM effects can be considered under threshold when the Raman effect is assumed at the threshold, since Raman effect dominates over Kerr effect in SOI technology. Finally, we guess that only one state of polarization for Stokes wave is at the threshold, while the other one is under-threshold. In this sense, the differential equations for under-threshold polarization state can be neglected. Although this last condition seems to be too restrictive, in a number of operative situations, it is really satisfied, as it will be demonstrated in the numerical results section. For compactness needs, we indicate with s^+ and s^- the co-propagating and counter-propagating Stokes waves with respect to the pump direction, respectively, with the polarization state candidate to be emitted. In order to determine the threshold relationship, it is convenient to formulate the complex amplitude coefficients as $a_i = u_i e^{j\phi_i}$. Consequently, two possible cases that are of interest occur:

2.2.1. CASE A) $A_{s+p}^{SRS} \cong A_{s-p}^{SRS}$

In this condition, the threshold values for both Stokes waves are very similar. Consequently, close to the threshold $u_{s+}^2 \cong u_{s-}^2 \cong 0$, TPA effects induced by Stokes waves can be neglected. Then, we can write

$$-\frac{N_c}{\tau_{eff}} + \frac{1}{2}\left[\frac{\beta_{pp}^{(TPA)}}{\hbar\omega_p\left(A_{pp}^{(TPA)}\right)^2}\left(u_p^4\right)\right] = 0 \tag{19}$$

$$j(\omega_{p,\bar{n}} - \omega_p)u_p e^{j\phi_p} - \frac{1}{2}\frac{1}{\tau_p}u_p e^{j\phi_p} - \frac{1}{2}v_{g,p}\alpha_p^{(FCA)}u_p e^{j\phi_p} - v_{g,p}\left[\frac{1}{2}\frac{\beta_{pp}^{TPA}}{A_{pp}^{TPA}}(u_p)^2\right]u_p e^{j\phi_p}$$
$$- v_{g,p}\left[\frac{1}{2}\frac{\lambda_s}{\lambda_p}g_{s+}^{eff}(u_{s+})^2 + \frac{1}{2}\frac{\lambda_s}{\lambda_p}g_{s-}^{eff}(u_{s-})^2\right]u_p e^{j\phi_p} + jv_{g,p}\frac{2\pi}{\lambda_p}\Delta n_p u_p e^{j\phi_p} + \xi_p S_p = 0 \tag{20}$$

$$j(\omega_{s\pm,\bar{l}} - \omega_{s\pm})u_{s\pm}e^{j\phi_{s\pm}} - \frac{1}{2}\frac{1}{\tau_s}u_{s\pm}e^{j\phi_{s\pm}} - \frac{1}{2}v_{g,s}\alpha_{s\pm}^{(FCA)}u_{s\pm}e^{j\phi_{s\pm}} - v_{g,s}\left[\frac{\beta_{s\pm p}^{TPA}}{A_{s\pm p}^{TPA}}u_p^2\right]u_{s\pm}e^{j\phi_{s\pm}}$$
$$+ v_{g,s}\left[\frac{1}{2}g_{s\pm}^{eff}u_p^2\right]u_{s\pm}e^{j\phi_{s\pm}} + jv_{g,s}\frac{2\pi}{\lambda_s}\Delta n_{s\pm}u_{s\pm}e^{j\phi_{s\pm}} - \frac{1}{2}b_{s\pm}u_{s\mp}e^{j\phi_{s\mp}} = 0. \tag{21}$$

Moreover, if the pump angular frequency ω_p is appropriately selected, it is possible to use the plasma effect to shift the pump frequency in such a way that it coincides with an angular resonance frequency of the optical cavity. In this condition, we can assume $\phi_{p+} = 2m\pi$, where m is an integer number. For the same reason, we can set $\phi_{s+} \cong \phi_{s-}$ obtaining, after some algebra, the following equation:

$$u_{1,2}^{p\to s\pm} = \sqrt{\frac{v_{g,s}\bar{g}_{s\pm} \pm \sqrt{(v_{g,s}\bar{g}_{s\pm})^2 - v_{g,s}\varsigma\sigma_s\rho_{s\pm}}}{v_{g,s}\sigma_s\varsigma}} \tag{22}$$

where

$$\overline{g}_{s\pm} = \left(-\frac{\beta_{s+p}^{TPA}}{A_{s\pm p}^{TPA}} + \frac{1}{2}g_{s\pm}^{eff}\right), \frac{1}{2}\rho_{s\pm} = \frac{1}{2}\frac{1}{\tau_s} + \frac{1}{2}b_{s\pm}, \quad \text{and} \quad \varsigma = \left[\tau_{eff}/(2\hbar\omega_p)\right]\left[\beta_{pp}^{(TPA)}\Big/\left(A_{pp}^{(TPA)}\right)^2\right].$$

The nomenclature $(p \to s\pm)$ in Eq. (22) indicates the pump amplitude value that induces the threshold for the forward $(+)$ or backward $(-)$ Stokes waves versus the pump direction. Finally,

substituting Eq. (22) in Eq. (20) and considering $u_{s+}^2 \cong u_{s-}^2 \cong 0$ (threshold condition), we obtain the following relationship for the value of S_p at the threshold:

$$P_{th1,th2}^{\pm} = \left|S_{1,2}^{p\to s\pm}\right|^2 = \left(\frac{1}{\xi_p}\right)^2 \left(\frac{1}{2}\frac{1}{\tau_p} u_{1,2}^{p\to s\pm} + \frac{1}{2} v_{g,p}\sigma_p\varsigma \left(u_{1,2}^{p\to s\pm}\right)^4 u_{1,2}^{p\to s\pm} + v_{g,p}\left[\frac{1}{2}\frac{\beta_{pp}^{TPA}}{A_{pp}^{TPA}}\left(u_{1,2}^{p\to s\pm}\right)^2\right] u_{1,2}^{p\to s\pm}\right)^2. \quad (23)$$

Thus, the two values of SRS threshold depend on both TPA and FCA effects (see the signs $+$ and $-$ under the root square of Eq. (22)). In addition, for a given coupling factor for the input pump κ_p^2, the upper threshold $(P_{th1}^{\pm})$ increases while the smaller threshold level $(P_{th2}^{\pm})$ decreases by decreasing κ_s^2. In contrast, for a given value of κ_s^2, both threshold levels increase by decreasing κ_p^2. However, for long cavities, the upper threshold $(P_{th1}^{\pm})$ assumes too large values. Consequently, hereinafter, we will consider only the second solution $P_{th2}^{\pm}$.

2.2.2. CASE B) $A_{s-p}^{SRS} < A_{s+p}^{SRS}$

This condition induces a lower threshold value for the backward Stokes wave with respect to the forward Stokes wave. Consequently, it is lawful to suppose that the following relationship is verified close to the threshold condition for s- wave: $u_{s-} \to 0$ and $u_{s+} = 0$. Similar to the previous case, we can neglect the TPA effects induced by the Stokes waves and write:

$$u_{1,2}^{p\to s-} = \sqrt{\frac{v_{g,s-}\bar{g}_{s-} \pm \sqrt{\left(v_{g,s}\bar{g}_{s-}\right)^2 - v_{g,s}\varsigma\sigma_s/\tau_s}}{v_{g,s-}\sigma_s\varsigma}} \quad (24)$$

$$P_{th1,th2}^{-} = \left|S_{1,2}^{p\to s-}\right|^2 = \left(\frac{1}{\xi_p}\right)^2 \left(\frac{1}{2}\frac{1}{\tau_p} u_{1,2}^{p\to s-} + \frac{1}{2} v_{g,p}\sigma_p\varsigma \left(u_{1,2}^{p\to s-}\right)^4 u_{1,2}^{p\to s-} + v_{g,p}\left[\frac{1}{2}\frac{\beta_{pp}^{TPA}}{A_{pp}^{TPA}}\left(u_{1,2}^{p\to s-}\right)^2\right] u_{1,2}^{p\to s-}\right)^2. \quad (25)$$

It is worth to note that, in this case, it is not possible to find the closed form solution for the forward Stokes wave threshold, because the presence of the backward Stokes wave above threshold induces some transcendental equations.

Thus, Eqs. (22) or (24) demonstrate that, by considering a real field amplitude of the input pump S_p and both real solutions $u_1^{p\to s\pm}$ $(u_1^{p+\to s-})$ and $u_2^{p\to s\pm}$ $(u_2^{p\to s-})$, SRS effect in the resonator can have a finite threshold only if the following relationships are verified:

$$\text{Case A)} \quad \left(v_{g,s}\overline{g}_{s\pm}\right)^2 \geq v_{g,s}\varsigma\sigma_s\rho_{s\pm} \quad (26.a)$$

$$\text{Case B)} \quad \left(v_{g,s}\overline{g}_{s-}\right)^2 \geq v_{g,s}\varsigma\sigma_s/\tau_s. \quad (26.b)$$

Therefore, Eqs. (26) imposes a limitation over the total cavity decay time τ_s for Stokes wave. In particular, it leads to find the upper limit for κ_s^2 value, which is compatible with the SRS effect threshold inside the microcavity resonator.

Consequently, Eqs. (26) state that the Stokes photon decay rate related to coupling must have an appropriate value in order to guarantee that the photon generation rate induced by SRS effect can compensate the overall photon decay rate due to linear losses, FCA, and coupling process. Finally, according to [34], the laser external efficiency η_{ex} has been estimated as

$$\eta_{ex} = e^{-\alpha_s L_{out}}\kappa_s^2\xi_p \frac{2}{g_p v_{g,p} u_2^{p\to s\pm}} \frac{1}{2\sqrt{P_{th2}^{\pm}}} \quad (27.a)$$

$$\eta_{ex} = e^{-\alpha_s L_{out}}\kappa_s^2\xi_p \frac{2}{g_p v_{g,p} u_2^{p\to s-}} \frac{1}{2\sqrt{P_{th2}^{-}}} \quad (27.b)$$

where α_s is the linear propagation loss inside the bus waveguide for Stokes wave, and L_{out} represents the waveguide length from the coupling region to the photodetector.

3. Numerical Results and Discussion

3.1. Design Rules

The goal of this sub-section is to analyze the features of the SRS emission by means of the effective Raman gain definition, previously proposed in Eq. (16). By this way, it will be possible to find the design guidelines for Raman lasers based on SOI race-track resonator. In this context, we briefly introduce the numerical solution adopted for the calculation of effective modal areas in case of TPA and SRS effects, as previously indicated in Eqs. (11)–(12). These modal areas represent very critical physical parameters in a silicon Raman laser, since $A_{i,j}^{TPA}$ is strictly related to the threshold power in the resonant cavity (see Eqs. (23) and (25)), as well as to the laser external efficiency η_{ex} (see Eqs. (27.a)-(27.b)), and $A_{s\rho\sigma,p}^{SRS}$ is related to the normalized effective SRS gain for the Stokes signal excitation (see Eqs. (14)–(16)). In this context, the algorithmic procedure for calculation of the effective modal areas has been implemented and investigated in detail using a full-vectorial FEM [39]. The main numerical problem encountered in these calculations consists in solving hybrid products (e.g., the scalar product $|\mathbf{e}_{s\rho\sigma} \cdot \mathbf{e}_p|^2$) occurring in Eqs. (11) and (12). In particular, with the term "hybrid," we mean the product of an electric field component associated to the pump optical mode propagating at λ_p (e.g., $\lambda_p = 1550$ nm) with an electric field component of the optical Stokes mode propagating at a different wavelength λ_s (e.g., $\lambda_s = 1686$ nm). Unfortunately, it is not possible to calculate integrals defined in Eqs. (11)–(12) by using any standard integral function available in the software, since the two quantities to be first multiplied and then integrated are calculated in two separate simulation domains because of the different operative wavelengths (i.e., two different eigenvalue problems, solved separately). Consequently, optical modes solved for the same waveguide but at different operative wavelengths cannot be processed simultaneously in the same simulation workspace.

To this aim, we have developed an algorithmic procedure based on saving in Matlab workspace the optical field mode distributions evaluated by Femlab. In particular, once all electric and magnetic field components of the optical mode calculated by the software are extracted [40] and all required variables are saved, data can be processed offline for general purposes (e.g., products and integrals), independently from the original simulation software. The main objective of the proposed approach is the necessity to develop a numerical tool for the integral calculus since all variables are processed out from the simulation software. Then, we have developed an algorithmic procedure for integral equations and implemented an optimization procedure in order to best fit our results with those calculated by the software. Obviously, this comparison can be executed only in case of non hybrid products (e.g., $|\mathbf{e}_p \cdot \mathbf{e}_p|^2$). In particular, a percent relative error function can be defined as

$$\varepsilon_{r,\delta}(\psi,\zeta) = \frac{A_{i,j}^{TPA}{}_{(software)} - A_{i,j}^{TPA}{}_{(algorithm)}}{A_{i,j}^{TPA}{}_{(software)}} \cdot 100[\%] \quad (i = j = \delta, \text{ with } \delta = s, p) \tag{28}$$

where ψ is the software parameter by which it is possible to set the number of mesh elements in the FEM simulation domain (i.e., the maximum element size scaling factor [39]), and ζ is the parameter related to the accuracy of the calculations (i.e., the element growth rate [39]). In Eq. (28), $A_{i,j}^{TPA}{}_{(software)}$ and $A_{i,j}^{TPA}{}_{(algorithm)}$ are the modal effective TPA areas calculated by the simulation software and our algorithmic procedure, respectively. In particular, the same error definition can be applied in case of modal effective SRS areas, resulting in identical numerical results. In fact, the relative error $\varepsilon_{r,\delta}(\psi,\zeta)$ introduced by our model is independent from the integral expression. Several iterations have been done in order to calculate the percent relative error as a function of different set of ψ and ζ, at both wavelengths λ_p and λ_s. In all simulations, an extremely fine mesh has been set consisting of a number of mesh elements ranging from $\sim$ 60 000 to $\sim$ 100 000, depending on

TABLE 1

Percent relative errors $\varepsilon_{r,\delta}(\psi,\zeta)\%$ calculated by optimization procedure applied to waveguides WG1 and WG2 at wavelengths $\lambda_p = 1550$ nm and $\lambda_s = 1686$ nm

	ζ			
	1.2	**1.05**	**1.001**	**1.0005**
ψ	**WG1: $\delta = p$ (pump), $\varepsilon_{r,p}(\psi,\zeta)$**			
0.15	0.53250090598002	0.57490687883856	2.04763477648778	1.35110702584469
0.125	0.20434385468702	0.30131223387034	1.57538470101592	0.54624435973488
0.1	0.63722324669439	0.69399800314440	1.17262881806181	1.27885914101735
	WG1: $\delta = s$ (Stokes), $\varepsilon_{r,s}(\psi,\zeta)$			
0.15	0.58692470168292	0.44280685042126	1.92482055411021	1.29962449898399
0.125	0.37636420985242	0.48752724448283	1.62537828425880	0.51390993360609
0.1	0.72943103033439	0.79641181377044	1.16059282188841	1.32444196722816
	WG2: $\delta = p$ (pump), $\varepsilon_{r,p}(\psi,\zeta)$			
0.15	0.09218335193882	0.09218335193882	4.38580482027508	2.96335414877718
0.125	2.99216193423012	2.72404437596221	6.13017724025040	5.89298986943261
0.1	0.22965866887604	1.34356700289419	3.54548329435845	4.43847067256604
	WG2: $\delta = s$ (Stokes), $\varepsilon_{r,s}(\psi,\zeta)$			
0.15	0.26937460341997	0.26937460342007	4.44659293607450	3.06364174269155
0.125	3.01636630634245	2.75732828105233	6.06929173574040	5.80925197921921
0.1	0.40124745223259	1.50635036498033	3.64476823520110	4.49703509522158

the parameter ψ. Moreover, other simulation parameters such as mesh curvature factor, i.e., mesh curvature cut-off and resolution of narrow regions, have been always set to their default values [39].

In Table 1, we report the numerical results of our optimization procedure applied in case of two different silicon rib waveguides (i.e., WG1 and WG2) at both pump and Stokes operative wavelengths (i.e., $\lambda_p = 1550$ nm and $\lambda_s = 1686$ nm). In particular, silicon waveguides are characterized by the following dimensions properly named according to the schematic shown in Fig. 1(b):

- WG1: $H_S = 300$ nm, $W = 700$ nm, $H = 500$ nm, $H_R = 200$ nm;
- WG2: $H_S = 180$ nm, $W = 700$ nm, $H = 500$ nm, $H_R = 320$ nm.

The aim of the optimization procedure consists in setting the couple (ψ,ζ) for which it is possible to obtain the minimum percent relative errors for the selected waveguide simultaneously at both wavelengths. In particular, for the waveguide WG1, the optimum couple is (0.125, 1.0005). In fact, by using this set of mesh parameters, the percent relative error is as small as $\sim$0.54% at λ_p and $\sim$0.51% at λ_s. Then, the error introduced in the calculation of hybrid scalar integrals is approximately the mean between those calculated in case of non hybrid ones at both wavelengths, in between $\varepsilon_{r,p}(\psi,\zeta)$ and $\varepsilon_{r,s}(\psi,\zeta)$. In conclusion, the couple (ψ,ζ) optimized for the waveguide WG2 is (0.1, 1.2), since the percent relative errors at wavelengths λ_p and λ_s are as small as $\sim$0.23% and $\sim$0.4%, respectively.

The validation of the integral calculus, based on the optimization procedure described above, has been tested by comparing our results with those proposed by Krause *et al.* in Ref. [37]. To this purpose, we have calculated normalized local Raman-gain efficiency (i.e., $g_{s\rho,\sigma} = 1/A^{SRS}_{s\rho\sigma,p}$) in a silicon photonic wire with width $W = 500$ nm, height $H = 220$ nm and surrounded by silica, as a function of the waveguide orientation θ ranging from 0° to 45°, for co-propagating and counter-propagating pump and Stokes waves. Moreover, the operative wavelength of the pump signal is $\lambda_p = 1455$ nm, while the wavelength of the Stokes signal is $\lambda_s = 1574$ nm. Numerical results plotted in Fig. 2 are in very good agreement with theoretical curves in Ref. [37], confirming our algorithmic procedure as a very efficient numerical tool for the calculation of both hybrid and non hybrid integrals.

The numerical procedure presented above has been generalized by considering the silicon rib waveguide sketched in Fig. 1(b). In particular, the normalized effective gain $(g^{eff}_{s\rho,\sigma}/g^{SRS}_{bulk})$ has been evaluated as a function of slab height H_S, for different polarization combinations between pump and Stokes waves, assuming $W = 700$ nm, $H = 500$ nm, $R_{shape} = 0.05$, and $\theta = 45°$. The pump beam

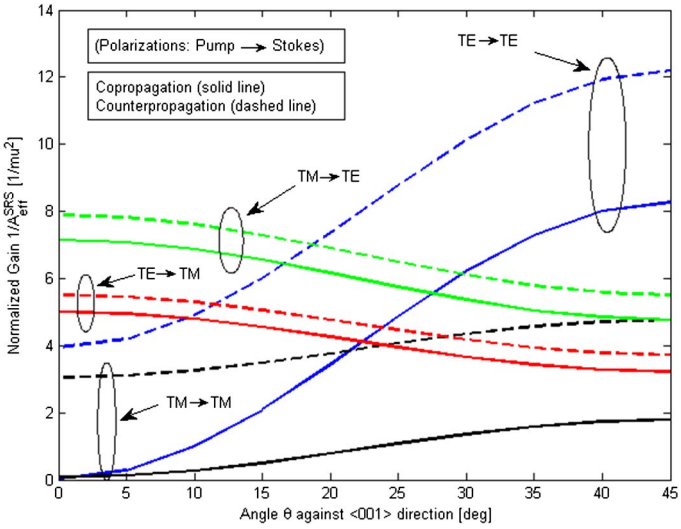

Fig. 2. Normalized gain in a silicon photonic wire (width W = 500 nm, height H = 220 nm) as a function of the waveguide orientation θ for co-propagating and counter-propagating pump and Stokes waves.

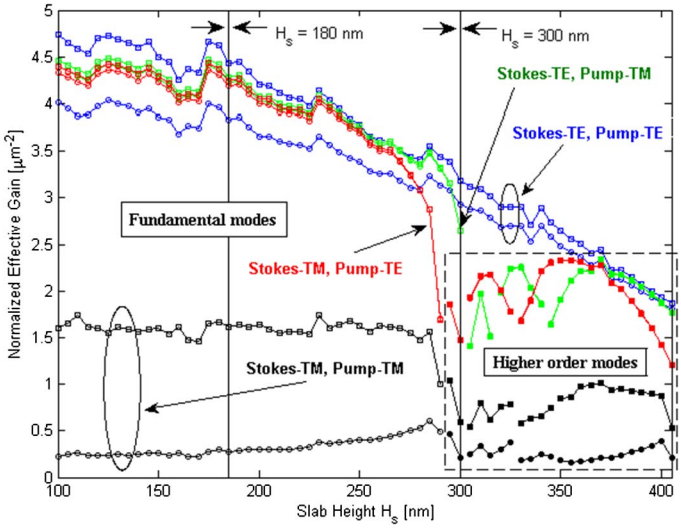

Fig. 3. Normalized effective gain as a function of slab height for different polarization state combinations.

is injected at 1550 nm, and the Stokes wavelength is originated at 1686 nm. Numerical results are plotted in Fig. 3. The plot clearly indicates that, for all values of slab height, the excitation $p_{TM} \rightarrow s^{\rho}_{TM}$ $(\rho = +, -)$ does not occur due to the very weak normalized effective gain, resulting in a negligible spontaneous emission efficiency for the polarization state combination $p_{TM} \rightarrow s^{\rho}_{TM}$. On the contrary, the other combinations exhibit relatively large values of $g^{eff}_{s\rho,\sigma}/g^{SRS}_{bulk}$, revealing a decreasing trend of the normalized effective gain as a function of increasing slab height H_S. In fact, the electric field distribution in the waveguide cross section is less confined by increasing H_S, resulting in a larger effective area for the SRS effect, as given by Eqs. (11)–(14). It is worth to outline the particular behavior for the excitation $p_{TE} \rightarrow s^{\rho}_{TE}$. As it is evident in Fig. 3, in the whole swept range of H_S, the normalized effective gain for the counter-propagating Stokes beam is larger than the co-propagating one. However, the difference between the two values decreases by increasing the slab height H_S. Then, in the case of $p_{TE} \rightarrow s^{\rho}_{TE}$ polarization state combination and for $H_S < 400$ nm, the excitation is always counter-propagating with respect to the pump wave, but at

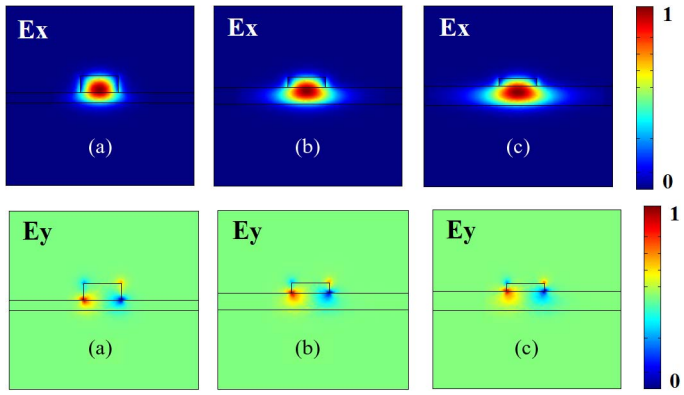

Fig. 4. Spatial distribution of the E_x- and E_y-field components of the fundamental quasi-TE optical mode for silicon rib waveguides with W = 700 nm, H = 500 nm and different slab height H_S = 180 nm (a), H_S = 300 nm (b) and H_S = 350 nm (c). λ_p = 1550 nm.

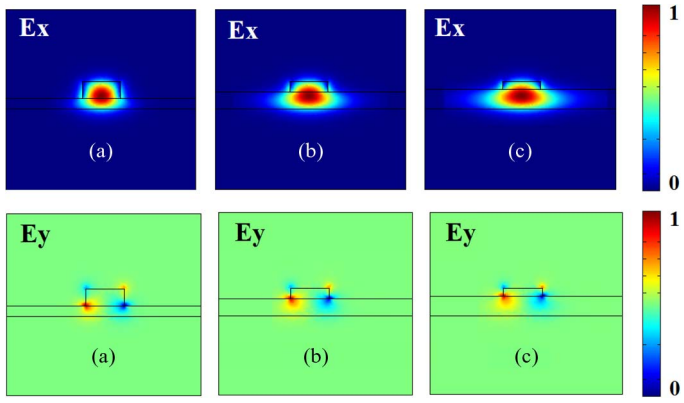

Fig. 5. Spatial distribution of the E_x- and E_y-field components of the fundamental quasi-TE optical mode for silicon rib waveguides with W = 700 nm, H = 500 nm and different slab height H_S = 180 nm (a), H_S = 300 nm (b) and H_S = 350 nm (c). λ_s = 1686 nm.

$H_S = 400$ nm, the Raman laser could emit in both directions since the difference between normalized effective gain for co-propagating and counter-propagating Stokes signals becomes negligible. However, in this last situation, the direction of emission should be uncertain, because it is influenced by the mode competition due to TPA effects induced by the growing Stokes waves.

Finally, it is worth to consider the excitations corresponding to the polarization state combinations $p_{TM} \rightarrow s^{\rho}_{TE}$ and $p_{TE} \rightarrow s^{\rho}_{TM}$. As it is evident, the behavior is quite similar in both operative conditions. In fact, the difference between the values of normalized effective gains $g^{eff}_{s\rho,\sigma}/g^{SRS}_{bulk}$ for co-propagating and counter-propagating Stokes beams is substantially negligible. Moreover, even in these cases, the directionality of the Stokes emission, in principle bidirectional, strongly depends on the mode competition between co- and counter-propagating Stokes signals. Anyway, the $p_{TE} \rightarrow s^{\rho}_{TE}$ excitation surely guarantees efficient single direction emission for a large range of H_S.

In order to complete the analysis of the silicon rib waveguide and the calculation of relative normalized effective gains for the Stokes signal excitation, we report the investigation on the optical mode spatial distributions for both quasi-TE and quasi-TM polarizations, for three rib waveguides characterized by $W = 700$ nm, $H = 500$ nm and different silicon slab heights H_S, i.e., 180 nm, 300 nm, and 350 nm. To this purpose, in Figs. 4 and 5, it is possible to observe the spatial distributions of E_x and E_y components of the quasi-TE polarized optical modes at pump and Stokes wavelengths. Simulation results confirm that quasi-TE fundamental modes are always supported by the silicon rib waveguide in the whole slab height range, extended from 100 nm to

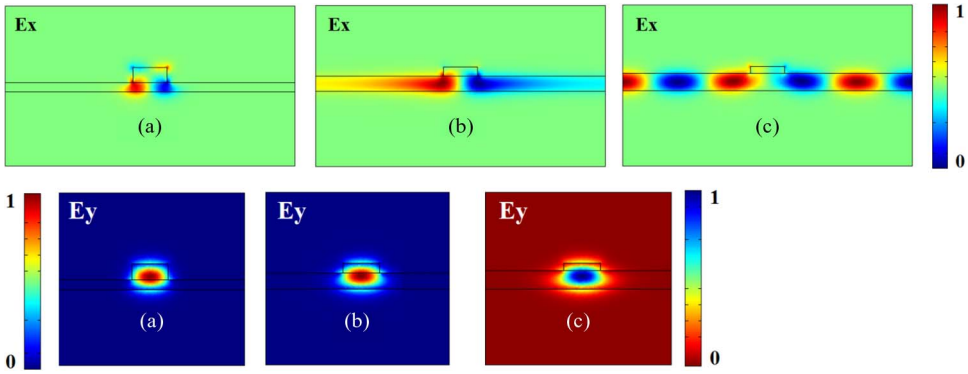

Fig. 6. Spatial distribution of the E_x- and E_y-field components of the fundamental quasi-TM optical mode for silicon rib waveguides with W = 700 nm, H = 500 nm and different slab height H_S = 180 nm (a), H_S = 300 nm (b) and H_S = 350 nm (c). λ_p = 1550 nm.

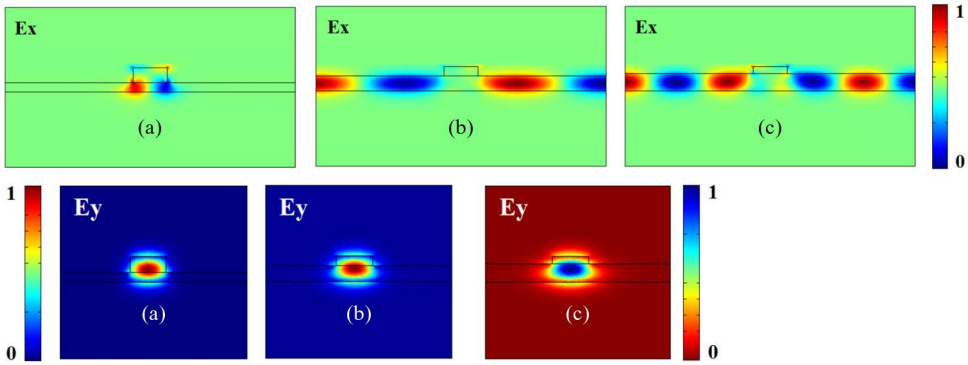

Fig. 7. Spatial distribution of the E_x- and E_y-field components of the fundamental quasi-TM optical mode for silicon rib waveguides with W = 700 nm, H = 500 nm and different slab height H_S = 180 nm (a), H_S = 300 nm (b) and H_S = 350 nm (c). λ_s = 1686 nm.

400 nm, at both wavelengths. However, the higher the slab, the lower the optical mode confinement in the silicon rib, resulting in a larger effective area for the SRS effect. Consequently, this behavior justifies the descending trends that characterize the normalized effective gains in case of co-propagating and counter-propagating Stokes signal emission, for the polarization state combination $p_{TE} \rightarrow s^{\rho}_{TE}$.

Simulation results calculated by FEM reveal a completely different behavior in case of quasi-TM polarized optical mode. In fact, in Figs. 6 and 7, it is possible to observe how the fundamental quasi-TM optical mode is supported only in silicon rib waveguides with a slab height $H_S = 180$ nm, while not for $H_S = 300$ nm and 350 nm. In fact, the calculated slab height limit values for the excitation of the fundamental quasi-TM mode in the silicon rib waveguide are $H_S = 300$ nm at the pump wavelength and $H_S = 290$ nm at the Stokes wavelength. Thus, it is useful to distinguish between two different conditions. The first one identifies all values of H_s that determine a weak optical confinement near the limit values mentioned above (i.e., $H_S = 290$ nm and 300 nm). To this aim, it is convenient to refer to Fig. 6(b), showing the spatial distribution of the E_x component of the fundamental quasi-TE optical mode in the rib waveguide with $H_S = 300$ nm (i.e., the limit value). In this case, the E_y component is fully confined into the rib waveguide, while the E_x component is partially distributed into the silicon slab, resulting in a decreasing normalized effective gain in case of $p_{TM} \rightarrow s^{\rho}_{TE}$, for both co-propagating and counter-propagating Stokes emissions according to Fig. 3. We have verified that a similar behavior characterizes both $p_{TE} \rightarrow s^{\rho}_{TM}$ and $p_{TM} \rightarrow s^{\rho}_{TM}$ excitations, with the limit value $H_S = 290$ nm.

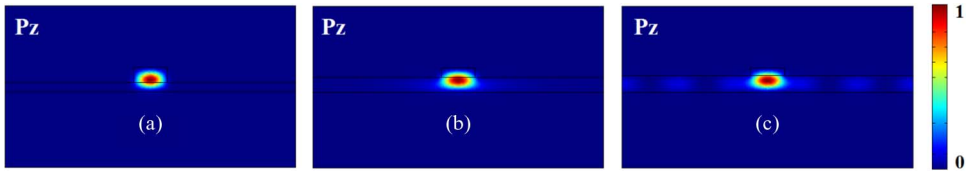

Fig. 8. Poynting power distribution into the x-y plane of the silicon waveguide cross-section with W = 700 nm, H = 500 nm and different slab height H_S = 180 nm (a), H_S = 300 nm (b) and H_S = 350 nm (c). λ_p = 1550 nm.

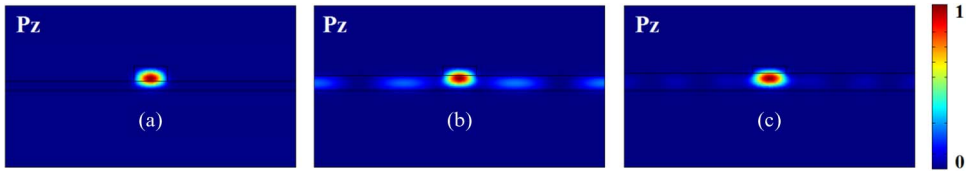

Fig. 9. Poynting power distribution into the x-y plane of the silicon waveguide cross-section with W = 700 nm, H = 500 nm and different slab height H_S = 180 nm (a), H_S = 300 nm (b) and H_S = 350 nm (c). λ_s = 1686 nm.

In Fig. 3, the region labeled as "Higher order modes" has been evidenced, to be distinguished from the region named "Fundamental modes." In fact, in all different polarization state combinations analyzed for the Stokes signal emission, with the only exception of $p_{TE} \rightarrow s^{\rho}_{TE}$, quasi-TM polarized higher order modes are excited into the silicon rib waveguide for slab values higher than the limit ones (i.e., $H_S = 290$ and $H_S = 300$), and the fundamental quasi-TM mode is not supported. To this purpose, in Figs. 6(b) and (c) and 7(c), it is evident how the E_x component of the optical mode presents uniformly distributed multiple lobes into the silicon slab, although the E_y component is well confined into the silicon rib. This condition results in low normalized effective gains associated to a number of higher order modes, as clearly shown in Fig. 3 in the squared region labeled as "Higher order modes."

In this context, the spatial distributions of the Poynting power of the quasi-TM polarized optical modes into the silicon waveguide cross-section are plotted in Figs. 8 and 9 as a function of different slab heights.

Numerical results confirm that high optical power confinement into the silicon rib waveguide can be still achieved in case of higher order modes. However, waveguide configurations characterized by slab heights higher than the limit values for the fundamental quasi-TM optical mode excitation, at both pump and Stokes wavelengths, are not useful for a strong Raman excitation, since the normalized effective gain is too low and the difference between the co-propagating and counter-propagating Stokes gains is quite negligible, resulting in an unpredictable Stokes mode competition.

Finally, simulations plotted in Fig. 3 with the investigation of the silicon waveguide considered in Figs. 4–9 represent a very useful tool to find the characteristic performance of Raman emission in race-track SOI resonator. In fact, this type of analysis allows to link the definition of the geometry of the racetrack resonator (i.e., R_{shape}) directly to the physical properties of the selected silicon waveguide, with the final task of defining the optimum waveguide architecture able to maximize the stimulated Raman emission.

In Fig. 10(a) and (b), the normalized effective gain is sketched as a function of the slab height for two different shape ratios, $R_{shape} = 0.01$ and $R_{shape} = 0.1$, respectively. All the other parameters are the same as before. We have assumed the pump wave aligned only with the quasi-TE mode. In particular, we can observe that both co-propagating and counter-propagating Stokes waves present a normalized effective gain which decreases with increasing the slab height H_s. This trend depends on the reduced confinement of the optical modes into the rib region, thus inducing a larger effective modal area. Thus, according to Eq. (24) or (25), we can conclude that the increase in the slab height

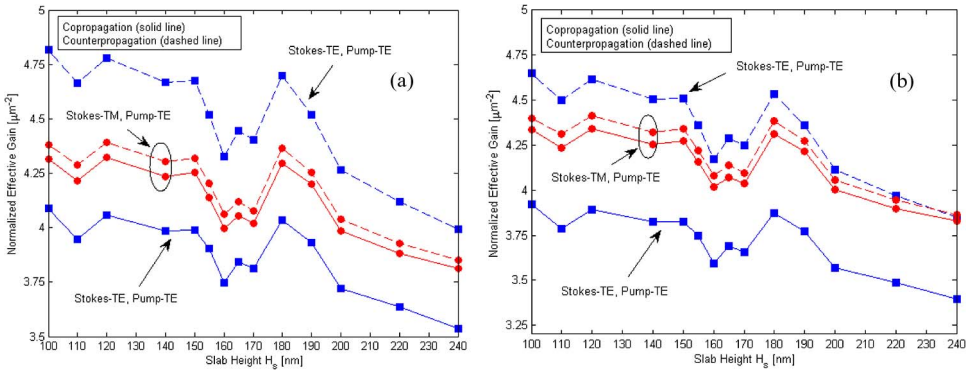

Fig. 10. Normalized effective gain as a function of slab height: (a) $R_{shape} = 0.01$; (b) $R_{shape} = 0.1$. Waveguide orientation $\theta = 45°$ with respect to the crystallographic axes in both graphs (a) and (b).

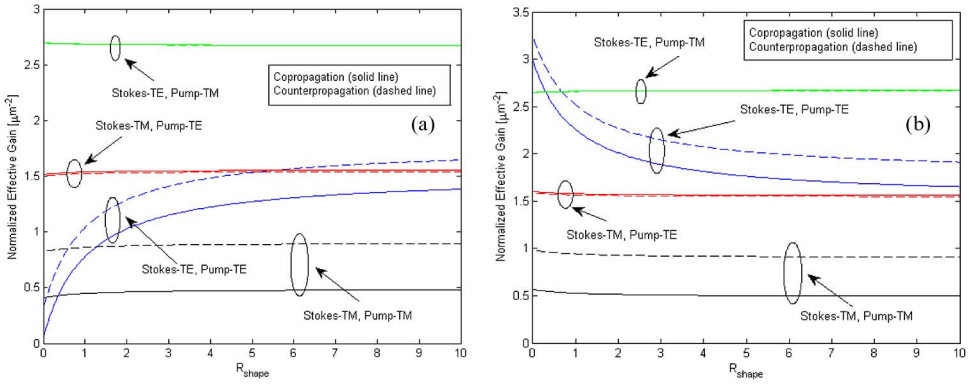

Fig. 11. Normalized effective gain as a function of the shape ratio for the waveguide WG1: (a) $\theta = 0°$, (b) $\theta = \pi/4$.

H_s induces, in its turn, an increase in the Raman laser threshold. In addition, it is evident that, for both shape ratios, the differences between the normalized effective gains associated to s^-_{TE} and s^+_{TE}, s^-_{TM} and s^+_{TM} Stokes waves are significant, being maximized in case of $p_{TE} \rightarrow s^{\rho}_{TE}$ emission. In addition, g^{eff}_{s-TE} assumes always higher values in the range of H_S from 100 nm to 240 nm, independently from the shape ratio of the race-track resonator. Moreover, larger values of R_{shape} induce a very weak shift toward lower values of $g^{eff}_{s\rho,\sigma}/g^{SRS}_{bulk}$. In summary, we can conclude that the counter-propagating Stokes waves are characterized by the highest values of $g^{eff}_{s\rho,\sigma}$, when injecting a quasi-TE polarized pump wave into the race-track resonator.

It is worth to outline that previous plots allow to individuate the emission features (i.e., co- or counter-propagating emission) for an a-priori fixed Stokes-pump polarization state combination only in terms of normalized effective gain. However, it is not possible to predict the effective polarization state of the Stokes beam emitted since the condition $g^{eff}_{s-TE} > g^{eff}_{s-TM}$ does not immediately implicate the emission of the quasi-TE polarized mode, depending on the coupling factor between the bus waveguides and the race-track resonator, too. In this context, it is evident how the physics of the Raman excitation into the silicon waveguide results to be strictly related to the geometry of guided-wave optical components, i.e., race-track resonator (i.e., R_{shape}), as well as directional couplers for the coupling of optical signals from input buses into the resonant cavity and *vice versa*. In order to demonstrate this last concept, hereinafter, we will consider the SOI waveguides named WG1 and WG2, as defined previously.

In Fig. 11(a) and (b), the normalized effective gain is shown as a function of the shape ratio for WG1, by considering all possible combinations between the polarization states of pump and Stokes

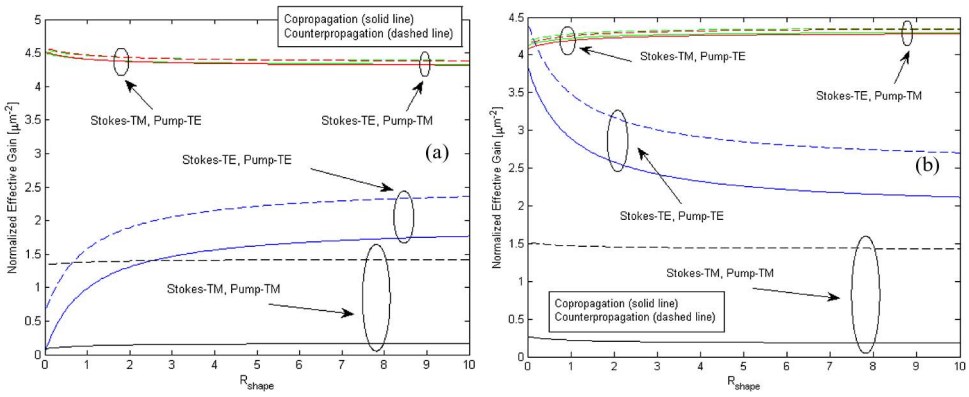

Fig. 12. Normalized effective gain as a function of shape ratio for waveguide WG2. a) $\theta = 0°$, b) $\theta = \pi/4$.

waves and assuming $\theta = 0$ and $\theta = \pi/4$, respectively. Two considerations are important. First, in case of $\theta = 0$, the excitation $p_{TE} \rightarrow s^{\rho}_{TE}$ is the only polarization state combination for which it is possible to observe curves monotonically increasing as a function of R_{shape}, with a saturation effect for $R_{shape} > 5$. In addition, all other cases exhibit a flat shape for both co-propagating and counter-propagating Stokes modes. Second, the excitation $p_{TM} \rightarrow s^{\rho}_{TE}$ maximizes the Raman gain, inducing high laser emission efficiency. Very interesting considerations can be also outlined for WG1 in case of $\theta = \pi/4$. In fact, Fig. 11(b) shows how the excitation $p_{TE} \rightarrow s^{\rho}_{TE}$ monotonically decreases as a function of R_{shape}, saturating for $R_{shape} > 5$. In addition, for $R_{shape} < 0.5$, the normalized effective gain for $p_{TE} \rightarrow s^{\rho}_{TE}$ is larger than for $p_{TM} \rightarrow s^{\rho}_{TE}$ excitation.

At this step of the analysis, we can demonstrate that larger Raman gains can be obtained with an appropriate selection of the waveguide orientation with respect to the crystallographic reference system (i.e., θ), shape ratio R_{shape}, pump polarization, and propagation direction of Stokes wave. However, curves plotted in Fig. 11 are not enough to completely predict the features of Stokes wave emitted by SRS effect, since other effects need to be included in the analysis, such as the signal coupling between the bus waveguide and the racetrack resonator.

The normalized effective gain as a function of the shape ratio is plotted in Fig. 12 for WG2. Despite of similar profiles characterizing curves plotted in Fig. 12(a) and (b) with respect to those in Fig. 11(a) and (b), some different physical features are worth to outline. In particular, although the waveguide WG1 presents normalized effective gain values $(g^{eff}_{s\rho,\sigma}/g^{SRS}_{bulk})$ for $p_{TE} \rightarrow s^{\rho}_{TE}$ excitation larger than those for $p_{TE} \rightarrow s^{\rho}_{TM}$ for each fixed value of R_{shape}, the waveguide WG2 exhibits comparable values of $g^{eff}_{s\rho,\sigma}/g^{SRS}_{bulk}$ for $R_{shape} < 0.5$. Consequently, it seems reasonable to assume that the Stokes emission will be counter-propagating, due to the large difference between $g^{eff}_{s-,TE}$ and $g^{eff}_{s-,TM}$, if the race-track resonator based on the waveguide WG1 is excited with a quasi-TE pump wave. However, the same conclusion is not suitable to WG2, for two reasons. The first one is that the difference between $g^{eff}_{s-,TE}$ and $g^{eff}_{s-,TM}$ depends on R_{shape}. In particular, for $R_{shape} > 0.5$, $g^{eff}_{s-,TM}$ dominates $g^{eff}_{s-,TE}$, being exactly the opposite trend with respect to WG1 case. Second, although we select $R_{shape} < 0.5$ resulting in $g^{eff}_{s-,TE} > g^{eff}_{s-,TM}$ (as in WG1), the difference between effective Raman gains is too small to predict the laser emission without including the coupling effects between the race-track resonator and the bus waveguides. In this context, a very useful coupling coefficient map for quasi-TE and quasi-TM polarized mode excitations for WG2 is plotted in Fig. 13, assuming the parameter set: $\theta = \pi/4$, $R_{shape} = 0.01$, $L_{cavity} = 2763\ \mu$m, and $0.05 < k^2_{p,TE} < 0.7$.

In the plot, the horizontal and vertical red lines represent the upper limit values of power coupling coefficients for quasi-TM and quasi-TE Stokes modes, respectively. In particular, for $k^2_{s,TM}$ and $k^2_{s,TE}$ lower than the aforementioned limits (i.e., $k^2_{s,TM} = 0.0817$ and $k^2_{s,TE} = 0.0828$), the SRS lasing occurs with threshold given in Eq. (26). Moreover, the diagonal black line divides the plane into two regions labeled as "TE-mode excitation" and "TM-mode excitation," where threshold levels satisfy the conditions $S_2^{p\rightarrow s-TE} < S_2^{p\rightarrow s-TM}$ and $S_2^{p\rightarrow s-TM} < S_2^{p\rightarrow s-TE}$, respectively. Consequently, for a

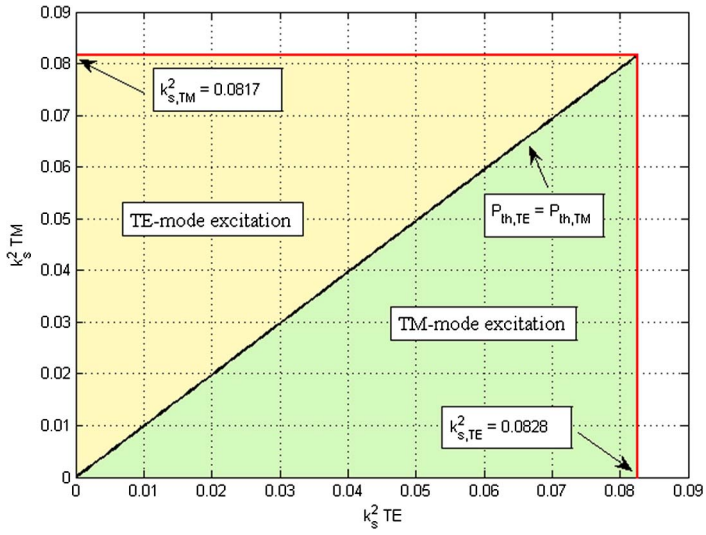

Fig. 13. Coupling coefficient map for waveguide WG2 with orientation $\theta = 45^\circ$ with respect to the crystallographic axes.

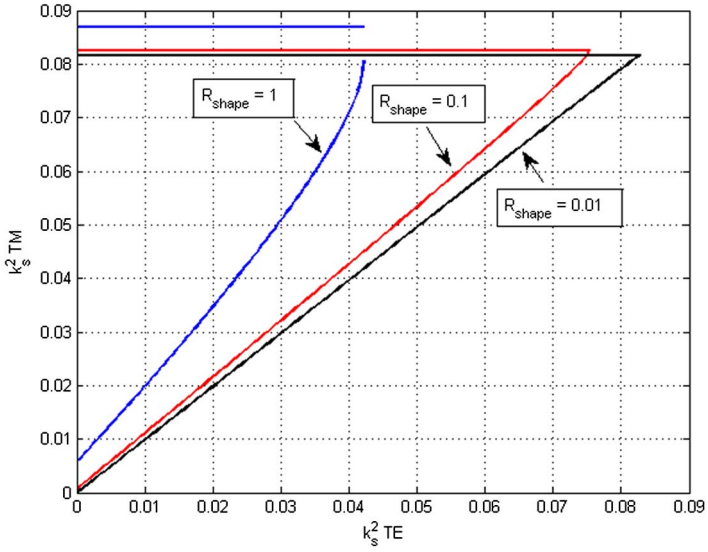

Fig. 14. Coupling coefficient map as a function of different values of the resonator shape ratio.

given couple of values $(k^2_{s,TE}, k^2_{s,TM})$ selected for the design of the directional coupler, the localization in the map univocally indicates the polarization state for the excited Stokes wave, which guarantees the lower threshold level. Therefore, the coupling coefficient map is a powerful tool to find the design guidelines for the directional coupler, with the goal to obtain a race-track resonator Raman laser with a specific polarization state.

In Fig. 14, the influence of the resonator shape ratio on the coupling coefficient map is shown. The plot clearly indicates that the TM-mode excitation region increases by increasing R_{shape} from 0.01 to 1.

For example, by considering the coupling coefficient sets ($k^2_{p,TE} = 0.4$, $k^2_{s,TE} = 0.02$, $k^2_{s,TM} = 0.06$, for quasi-TE excitation) and ($k^2_{p,TE} = 0.4$, $k^2_{s,TE} = 0.05$, $k^2_{s,TM} = 0.03$, for quasi-TM excitation), we have simulated the Stokes signal excitation with a pump power of 100 mW, launched in the input

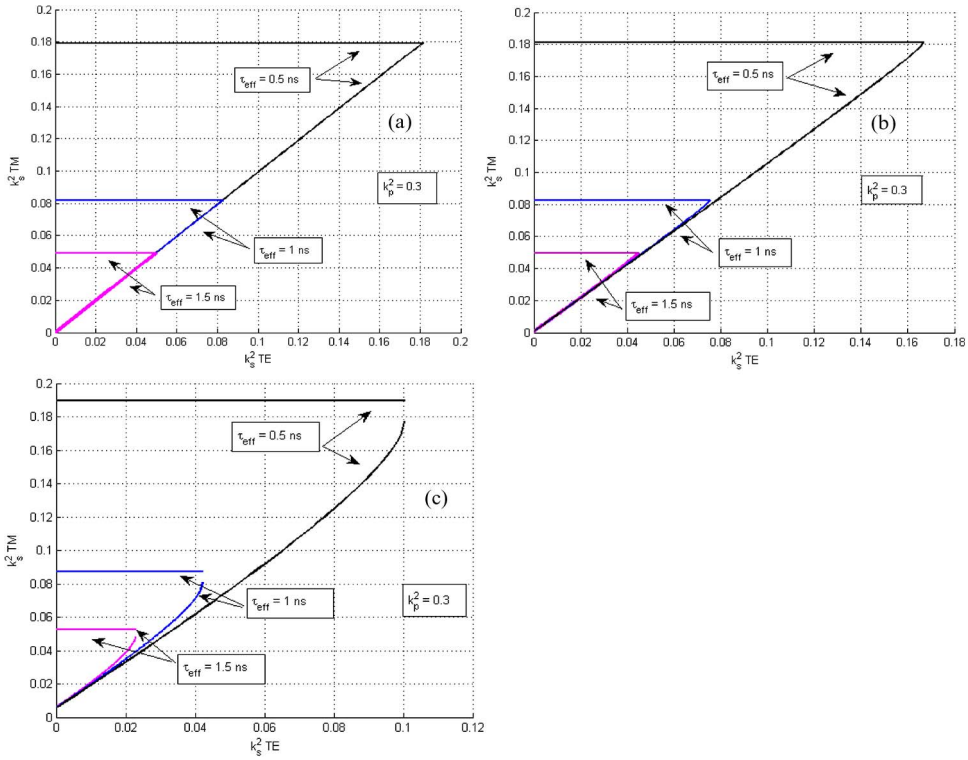

Fig. 15. Coupling coefficient map for different values of the effective recombination lifetime: (a) $R_{shape} = 0.01$, (b) 0.1, (c) 1.

bus waveguide. In particular, in case of $R_{shape} = 0.01$, the power of the quasi-TE-polarized Stokes signal is 1 mW, while the power of quasi-TM polarized Stokes signal is 2 mW. Moreover, in case of $R_{shape} = 0.1$ and $R_{shape} = 1$, calculated output powers associated to quasi-TE and quasi-TM polarized Stokes signals are $P_{out,TE} = 2.03$ mW, $P_{out,TE} = 2.15$ mW and $P_{out,TM} = 0.9$ mW, $P_{out,TM} = 0.45$ mW, respectively.

Thus, both Figs. 13 and 14 are critical for the design of Raman lasers based on SOI race-track resonator. In fact, once the waveguide cross-section is defined, plots similar to those shown in Fig. 12 can be used for selecting the optimum race-track geometry and identifying the polarization state and the emission directionality of the laser. Consequently, the coupling coefficient map (see Figs. 13 and 14) individuates the requirements for the directional coupler design in order to select the desired Stokes polarization states.

In Figs. 15(a)–(c), the coupling coefficient maps calculated for different effective recombination times and shape ratios are plotted, by considering waveguide WG2 and assuming $\theta = \pi/4$, $L_{cavity} = 2763$ μm, and $k_p^2 = 0.3$. As it is possible to observe, by increasing τ_{eff}, both the excitation regions decrease, as induced by the lowering of the upper limit value for k_s^2, according to the relationship in Eq. (26). The value of τ_{eff} can be controlled by the reverse voltage applied to the p-i-n silicon waveguide, as investigated in the systematic analysis proposed in Ref. [47].

3.1.1. Directional Coupler Design

The design of symmetrical directional couplers based on silicon rib waveguides (i.e., WG1 and WG2) has been modeled by employing both full-vectorial FEM [39] and CMT [48]–[50], supported by the three-dimensional (3D) beam propagation method (BPM) [51]. The calculation of symmetric and anti-symmetric supermodes in silicon rib waveguides by full-vectorial FEM has been carried out in order to jointly apply the supermodes approach and CMT for the calculation of coupling lengths L_c and power coupling coefficients (i.e., $k_{i,j}^2$ with $i = s, p$ and $j =$ TE, TM) for both waveguides WG1

TABLE 2

Fitting parameters for waveguides WG1 and WG2 at both pump and Stokes wavelengths and TE and TM optical mode polarizations

Waveguide	Polarization	Wavelength λ [nm]	Fitting Parameters A [μm]	B [μm^{-1}]
WG1	TE	1550	10.9823	4.2479
WG1	TE	1686	9.55	4.1793
WG2	TE	1550	21.0154	6.3674
WG2	TE	1686	18.0899	5.7080
WG2	TM	1550	7.5507	10.9877
WG2	TM	1686	6.4216	10.0547

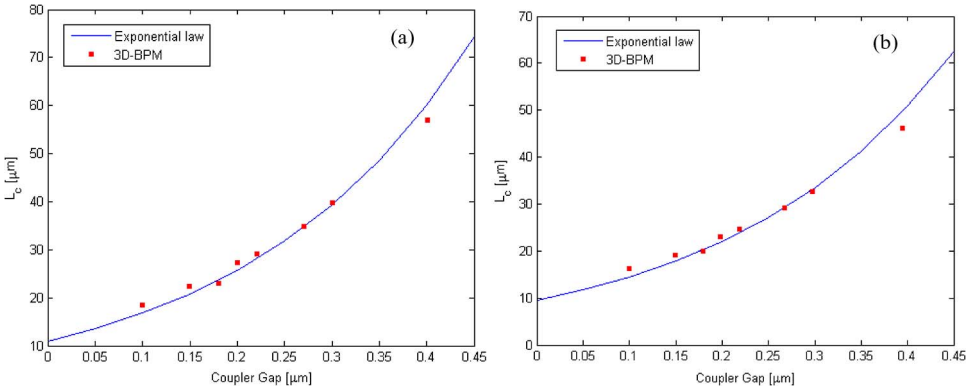

Fig. 16. Fitting results for waveguide WG1 in case of quasi-TE optical mode at pump (a) and Stokes (b) wavelengths.

and WG2, as a function of directional coupler gaps, g. Furthermore, the coupling length is a function of the directional coupler gap by the typical exponential law as

$$L_c = Ae^{Bg} \tag{29}$$

where A and B are fitting parameters to be found in order to best fit numerical results of L_c corresponding to different directional coupler gaps simulated by FEM.

Fitting parameters are summarized in Table 2 by considering TE and TM optical mode polarizations, as well as both pump and Stokes wavelengths. The numerical procedure described until now has been validated by simulating some directional coupler configurations (e.g., $g = 0.1$ μm, 0.15 μm, 0.2 μm, to name a few) through the 3D-BPM propagator and comparing results as plotted in Figs. 16–18, revealing a very good agreement for both waveguides and TE and TM polarizations, at the operative wavelengths λ_p and λ_s.

3.2. Model Validation

The mathematical model developed and discussed until now and the physical assumptions for the Raman laser effect induced in microcavities have been tested by comparing our numerical results with some experiments proposed in literature. A very interesting set of comparisons with experimental results involves the CW Raman laser based on SOI resonator. The architecture used in the experimental setup proposed by Rong *et al.* in Ref. [33] is similar to that considered here as based on a SOI racetrack resonator, but it is characterized by only one input/output bus waveguide. To this purpose, in our simulations, we have properly removed the bottom bus according to the schematic previously shown in Fig. 1. The proposed device is characterized by a p-i-n silicon rib waveguide with the following geometrical parameters: width $W = 1.5$ μm, overall height $H = 1.55$ μm, rib etch depth $H_R = 0.76$ μm, and slab height $H_S = 790$ nm. In our validation test, we have considered two different cavities having racetrack-ring total lengths of $L_{cavity} = 3$ cm and

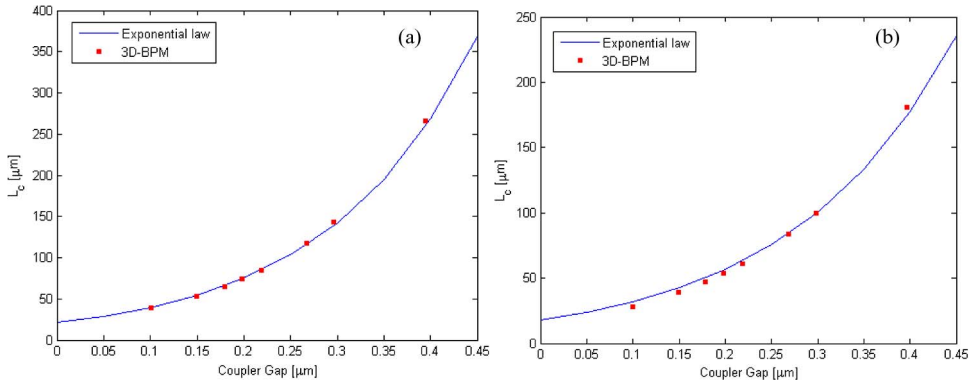

Fig. 17. Fitting results for waveguide WG2 in case of quasi-TE optical mode at pump (a) and Stokes (b) wavelengths.

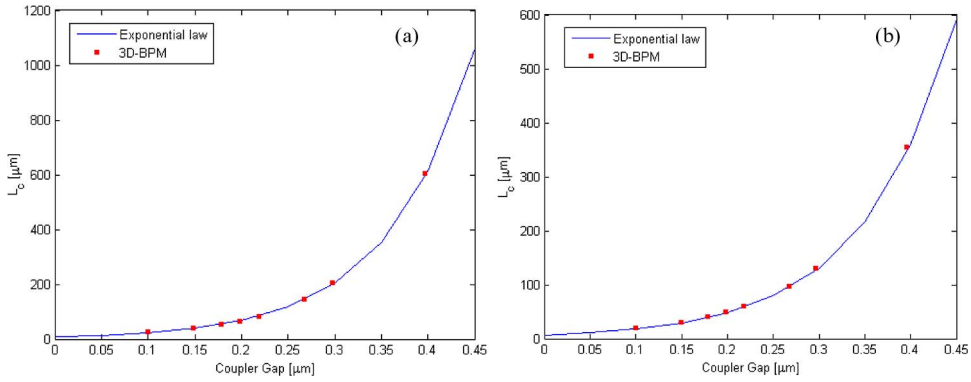

Fig. 18. Fitting results for waveguide WG2 in case of quasi-TM optical mode at pump (a) and Stokes (b) wavelengths.

TABLE 3

Physical parameters used in our model for the validation test with experiments presented in Ref. [33] (pump at $\lambda_p = 1550$ and Stokes at $\lambda_s = 1686$ nm)

PARAMETERS	ASSUMED VALUES
α_p	0.6 (dB/cm)
α_s	0.6 (dB/cm)
σ_0	1.45×10^{-21} (m^2)
σ_p	1.45×10^{-21} (m^2)
σ_s	1.7156×10^{-21} (m^2)
$n_{2,Si}$	6×10^{-18} ($m^2\cdot W^{-1}$) @ 1.55 μm
$n_{2,SiO2}$	3.2×10^{-20} ($m^2\cdot W^{-1}$) @ 1.55 μm
β^{TPA}	5×10^{-12} (m/W)
τ_{eff}	depending on applied reverse bias voltage
g_{bulk}^{SRS}	9.5×10^{-11} (m/W)

1.5 cm, respectively. Both devices are based on the same silicon rib waveguide described above, and characterized by a bend radius of 400 μm. Finally, the measured optical parameters presented in Ref. [33] and used in our simulations are listed in Table 3. In the experiments, Raman laser devices have been also tested by considering different reverse bias voltages applied to the p-i-n silicon rib waveguide. Moreover, different coupling factors for pump and Stokes waves have been considered, too. To this purpose, Fig. 19(a) and (b) shows the laser output power P_{out} versus P_{in} (pump input power) as a function of the following reverse bias voltages: 0, 5, 10, and 25 V.

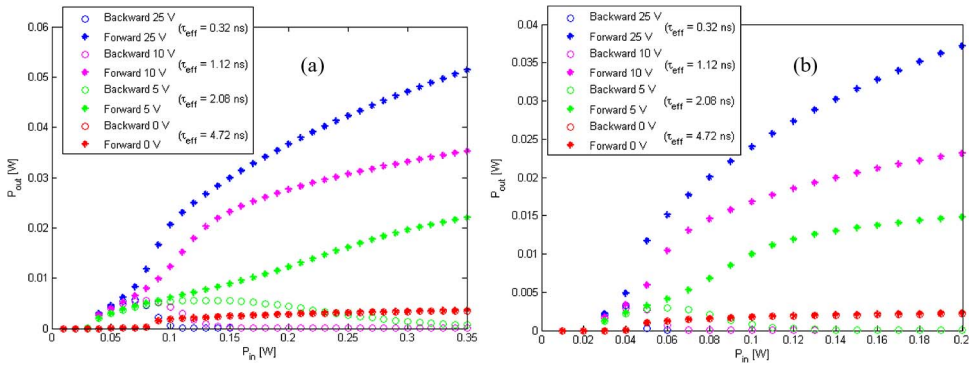

Fig. 19. Simulation results of the Raman laser presented in Ref. [33] characterized by different cavity lengths $L_{cavity} = 3$ cm (a) and $L_{cavity} = 1.5$ cm (b), as a function of reverse bias voltages applied to the p-i-n silicon rib waveguide.

Moreover, as indicated in Table 3, the effective free carrier lifetime changes as a function of the applied reverse bias voltage, as depicted in the legend in Fig. 19. In conclusion, in case of a cavity length $L_{cavity} = 3$ cm, the coupling coefficients considered in simulations are $\kappa_p^2 = 0.3$ for pump at $\lambda_p = 1550$ nm and $\kappa_s^2 = 0.12$ for Stokes signal at $\lambda_s = 1686$ nm, while for $L_{cavity} = 1.5$ cm, coupling coefficients are $\kappa_p^2 = 0.43$ and $\kappa_s^2 = 0.063$, respectively.

The plots shown in Fig. 19(a) and (b) exhibit a very good agreement with the experimental data published in [33], in terms of threshold values, output powers above thresholds, and external efficiencies. Moreover, arbitrary fitting parameters have not been used. Finally, our investigations indicate that the Raman emission is aligned as quasi-TM mode, resulting to be co-propagating with respect to the pump wave. In particular, in case of cavity length $L_{cavity} = 3$ cm, measured threshold power with a reverse bias voltage equal to 25 V is as low as 20 mW [33], with a maximum output power of about 50 mW, revealing a good agreement with our numerical results plotted in Fig. 19(a).

3.3. Raman Laser Performance

In this sub-section, we present a number of numerical results on the performance exhibited by Raman laser based on a SOI race-track resonator, calculated by numerically solving the system of Eqs. (4)–(8) and (17) and applying Eqs. (23), (25), and (27) as a validation test. For the following simulations, WG1 and WG2 waveguides are assumed, with physical and geometrical parameters calculated and listed in Table 4. Furthermore, other significant parameters assumed in our simulations, such as propagation losses at both pump and Stokes operative wavelengths, non-linear parameters, effective recombination lifetime for free carriers, to name a few, are summarized in Table 5.

Fig. 20(a) and (b) show the external emission efficiency and the threshold power, respectively, as a function of the coupling factors for pump (κ_p^2) and Stokes (κ_s^2) waves. The 3D plots have been performed for WG1 by assuming a cavity length $L_{cavity} = 2763$ μm and a resonator shape ratio $R_{shape} = 0.01$, resulting in the following effective SRS gains: $g^{eff}_{s_{-TE}p_{TE}} = 340.1215$ $[\mathrm{W \cdot m}]^{-1}$ and $g^{eff}_{s_{+TE}p_{TE}} = 312.7744$ $[\mathrm{W \cdot m}]^{-1}$. According to the previous discussion, the Stokes emission is backward with respect to the pump with a quasi-TE polarization state. Fig. 20(a) shows that the efficiency increases by increasing κ_p^2 for a given κ_s^2. On the contrary, for a given value of κ_p^2, the external efficiency versus κ_s^2 presents a maximum.

In addition, Fig. 20(b) shows an opposite trend for the threshold power. In fact, it is possible to observe a decreasing profile as a function of decreasing κ_s^2, with a given value of κ_p^2.

Moreover, for larger values of κ_s^2, the threshold power exhibits a minimum as a function of κ_p^2. A maximum external efficiency can be estimated as high as $\eta_{ex} = 23\%$, with $\kappa_p^2 = 0.4$ and $\kappa_s^2 = 0.05$. Similar simulations have been performed by assuming $R_{shape} = 0.1$ (i.e., $g^{eff}_{s_{-TE}p_{TE}} = 327.5638$ $[\mathrm{W \cdot m}]^{-1}$ and $g^{eff}_{s_{+TE}p_{TE}} = 300.2167$ $[\mathrm{W \cdot m}]^{-1}$) and $R_{shape} = 1$ (i.e., $g^{eff}_{s_{-TE}p_{TE}} = 264.1870$ $[\mathrm{W \cdot m}]^{-1}$ and $g^{eff}_{s_{+TE}p_{TE}} = 236.8399$ $[\mathrm{W \cdot m}]^{-1}$), resulting in a maximum efficiency of 22% (with $\kappa_p^2 = 0.4$ and

TABLE 4

Physical and geometrical waveguide parameters calculated through our model, by assuming the pump at $\lambda_p = 1550$ nm and the Stokes signal at $\lambda_s = 1686$ nm

	H_S (nm)	H_R (nm)	W (nm)	H (nm)	$n_{eff,p}$	$n_{eff,s}$	$v_{g,p}$ (m/s)	$v_{g,s}$ (m/s)	$\beta_{1,p}$ (s/m)	$\beta_{1,s}$ (s/m)
WG1										
TE*	300	200	700	500	3.1650	3.1108	7.912×10^{7}	7.937×10^{7}	1.264×10^{-8}	1.259×10^{-8}
WG2										
TE*	180	320	700	500	3.1125	3.0467	7.765×10^{7}	7.758×10^{7}	1.288×10^{-8}	1.289×10^{-8}
TM*	180	320	700	500	-	2.9230	-	7.320×10^{7}	-	1.366×10^{-8}

TPA Effective Areas: $A_{i,j}^{TPA}$ (μm^2)

WG1									
-	$A_{p,p}$	$A_{s+,s+}$	$A_{s-,s-}$	$A_{s-,p}$	$A_{s+,p}$	PUMP (TE) –STOKES (TE)			
Si	0.3094	0.3265	0.3265	0.3180	0.3180				
SiO_2	113.04	83.361	83.361	96.354	96.354				
WG2									
-	$A_{p,p}$	$A_{s+,s+}$	$A_{s-,s-}$	$A_{s-,p}$	$A_{s+,p}$	PUMP (TE) –STOKES (TE)			
Si	0.2317	0.2416	0.2416	0.2367	0.2367				
SiO_2	91.615	65.173	65.173	76.894	76.894				
-	$A_{p,p}$	$A_{s+,s+}$	$A_{s-,s-}$	$A_{s-,p}$	$A_{s+,p}$	PUMP (TE) –STOKES (TM)			
Si	0.2317	0.2325	0.2325	0.6317	0.6317				
SiO_2	91.615	8.786	8.786	61.531	61.531				

-	$A_{s-TE,\,s-TM}$	$A_{s-TE,\,s+TM}$	$A_{s-TM,\,s-TE}$	$A_{s-TM,\,s+TE}$	$A_{s+TE,\,s-TM}$	$A_{s+TE,\,s+TM}$	$A_{s+TM,\,s-TE}$	$A_{s+TM,\,s+TE}$	PUMP (TE)
Si	63.062	63.99	63.062	63.99	63.99	63.99	63.99	63.99	
SiO2	47.342	51.413	51.413	51.413	51.413	51.413	51.413	51.413	

*The polarization is referred to the Stokes signal, since the pump one is always quasi-TE polarized.

TABLE 5

Physical parameters for Stokes excitation in SOI racetrack resonator at wavelengths $\lambda_p = 1550$ and $\lambda_s = 1686$ nm

PARAMETERS	ASSUMED VALUES†
α_p	0.5 (dB/cm)
α_s	0.5 (dB/cm)
σ_0	1.45×10^{-21} (m^2)
σ_p	1.45×10^{-21} (m^2)
σ_s	1.7156×10^{-21} (m^2)
$n_{2,Si}$	6×10^{-18} ($m^2\cdot W^{-1}$) @ 1.55 μm
$n_{2,SiO2}$	3.2×10^{-20} ($m^2\cdot W^{-1}$) @ 1.55 μm
$N_{c,0}$	10^{20} (m^{-3})
β^{TPA}	5×10^{-12} (m/W)
τ_{eff}	1×10^{-9} (s)
R_{back}	10^{-4}
g_{bulk}^{SRS}	10.5×10^{-11} (m/W)

† All parameters are the same for both WG1 and WG2 waveguides.

$\kappa_s^2 = 0.03$) or 17% (with $\kappa_p^2 = 0.4$ and $\kappa_s^2 = 0.018$). Moreover, by increasing the resonator shape ratio, it is possible to observe a reduction in the external efficiency and, simultaneously, a lower threshold power level for the Raman laser. Furthermore, it is worth to note that previous results have been achieved by using the design relationships given in Eqs. (23), (25), and (27). To confirm the correctness and strength of Eqs. (23), (25), and (27), we have solved without any a-priori assumption the system of Eqs. (4)–(8) and (17) in CW regime for different values of input quasi-TE pump power. Thus, Fig. 21 shows the laser output power versus the input pump power, assuming a cavity length $L_{cavity} = 2763$ μm, a resonator shape ratio $R_{shape} = 0.01$, and power coupling coefficients $\kappa_{p,TE}^2 = 0.4$, $\kappa_{s,TE}^2 = 0.05$. In the following simulations, the output laser power has been calculated at the end of the bus waveguide with length of 150 μm and a coefficient loss of about 0.5 dB/cm.

It is evident how the unique solution different from zero is the quasi-TE backward Stokes wave, thus confirming the physical discussions and predictions made in the previous sub-section. In addition, Fig. 21(a) gives the threshold power as $P_{th2}^{-} \cong 0.15$ W and the external efficiency (curve

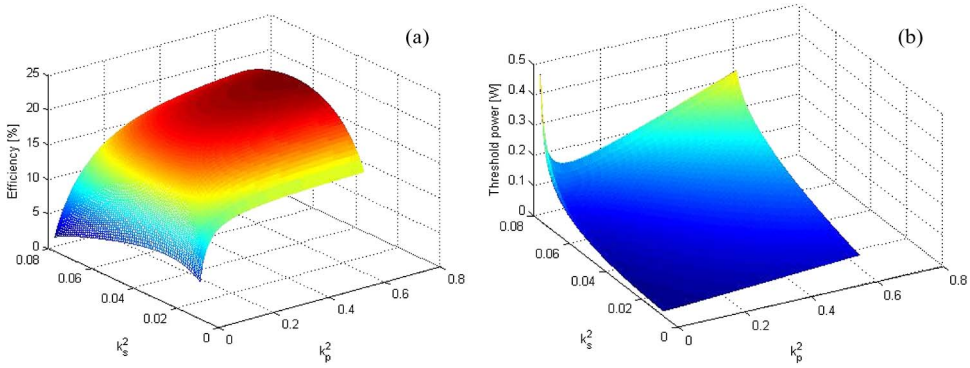

Fig. 20. External emission efficiency (a) and threshold power (b) versus the pump and Stokes coupling factors.

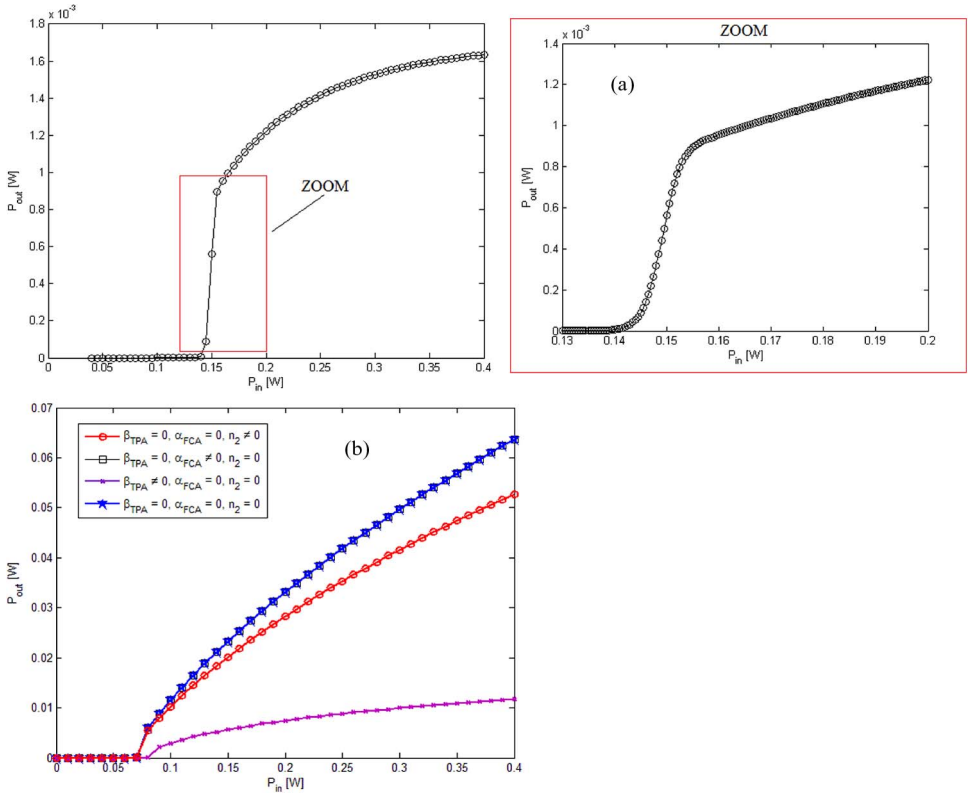

Fig. 21. Output power of the quasi-TE polarized Stokes backward signal as a function of input pump power (a) with all non-linear effects (b) with some non-linear effects.

slope close to the threshold) as high as $\eta_{ex} \cong 22\%$, in good agreement with values previously obtained in Fig. 20. Moreover, the curve in Fig. 21(a) shows a saturation as due to TPA effect induced by both pump and Stokes waves. Then, at the saturation, the output laser power is 1.6 mW for an input power of 0.4 W. Similar simulations have been performed for $R_{shape} = 0.1$ and $R_{shape} = 1$, resulting in output laser powers of 1.58 mW and 0.5 mW, respectively. Then, the saturation induced by TPA increases by increasing the resonator shape ratio. Fig. 21(b) well clarifies the influence of the nonlinear effects considered in the model. In particular, we have simulated the output Raman laser power versus the input pump power considering each effect step

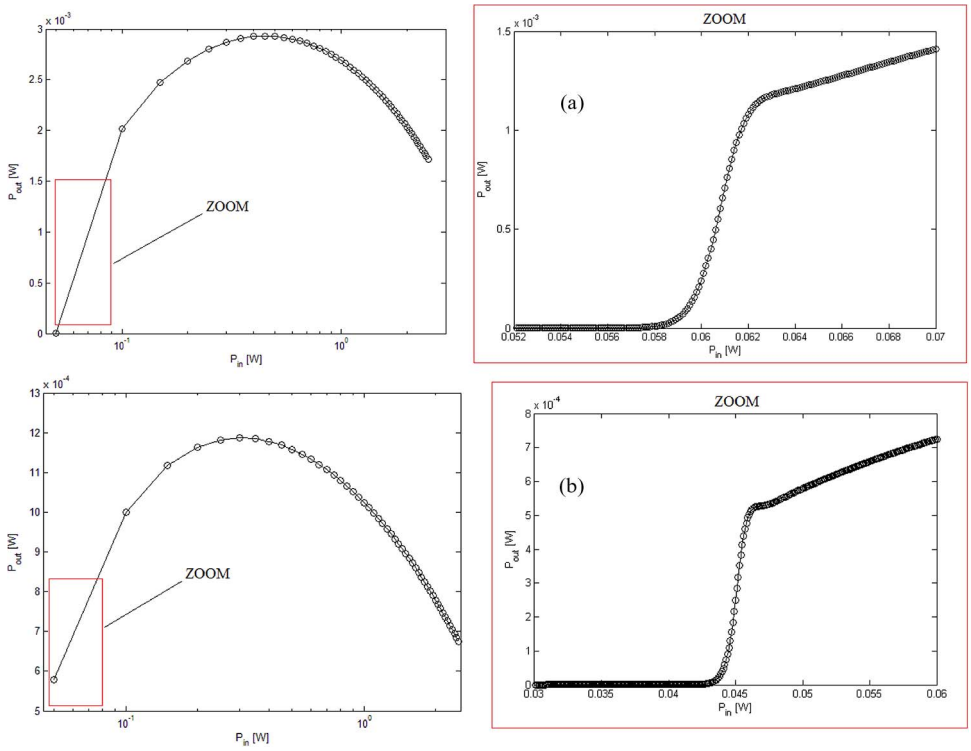

Fig. 22. Output laser power versus the input pump power: (a) quasi-TM backward Stokes wave; (b) quasi-TE backward Stokes wave.

by step. We can observe that the largest detrimental effect is induced by TPA. In fact, the only presence of TPA induces larger threshold and lower quantum efficiency than in all other cases. Moreover, blue and black curves are perfectly overlapped, revealing that FCA alone has a negligible influence. Thus, FCA shows its detrimental effect only occurring together with TPA. Finally, the only presence of Kerr effect does not influence both the threshold level and the quantum efficiency, but it reduces the output Raman laser power with increasing more and more the input pump power.

Furthermore, it is worth to show similar simulations performed for WG2, as in Fig. 22, where $L_{cavity} = 2763\ \mu$m, $R_{shape} = 0.01$ (i.e., $g^{eff}_{s_{-TE}p_{TE}} = 464.2749\ [\mathrm{W \cdot m}]^{-1}$, $g^{eff}_{s_{+TE}p_{TE}} = 402.4356\ [\mathrm{W \cdot m}]^{-1}$, $g^{eff}_{s_{-TM}p_{TE}} = 435.4718\ [\mathrm{W \cdot m}]^{-1}$, $g^{eff}_{s_{+TM}p_{TE}} = 429.0462\ [\mathrm{W \cdot m}]^{-1}$), $\kappa^2_{p,TE} = 0.4$, ($\kappa^2_{s,TE} = 0.05$, $\kappa^2_{s,TM} = 0.03$ - case (a)), and ($\kappa^2_{s,TE} = 0.02$, $\kappa^2_{s,TM} = 0.06$ - case (b)). The solutions of the system of Eqs. (4)–(8) and (17), plotted in Fig. 22, show the lasing effect for backward quasi-TM Stokes wave (a) and backward quasi-TE Stokes wave (b). These results are in very good agreement with the prevision derived from the coupling coefficient map (see Fig. 13). In fact, it is easy to check that the couple of values ($\kappa^2_{s,TE} = 0.05$, $\kappa^2_{s,TM} = 0.03$) localizes a point in the TM-mode excitation region. On the contrary, the values ($\kappa^2_{s,TE} = 0.02$, $\kappa^2_{s,TM} = 0.06$) match a point in the TE-mode excitation region. In addition, the quasi-TM emission presents a larger value of external efficiency as high as 21% with respect to quasi-TE mode (i.e., $\eta_{ex} < 10\%$). On the contrary, the backward Stokes quasi-TM wave has a threshold level of 0.05 W, higher than the quasi-TE emission (i.e., $\sim$0.043 W). Finally, a Raman laser based on waveguide WG2 gives similar values of external efficiency but lower threshold powers and higher output laser powers with respect to that based on WG1. This is particularly due to the larger SRS effect in highly confined waveguides.

A very useful analysis is presented in Figs. 23 and 24. The output Stokes power evaluated at the end of the waveguide bus, with length of 150 μm and coefficient loss of 0.5 dB/cm, has been simulated as a function of different cavity lengths and R_{shape}, by considering a constant pump optical power (350 mW) over the threshold level, in case of both waveguide configurations, i.e.,

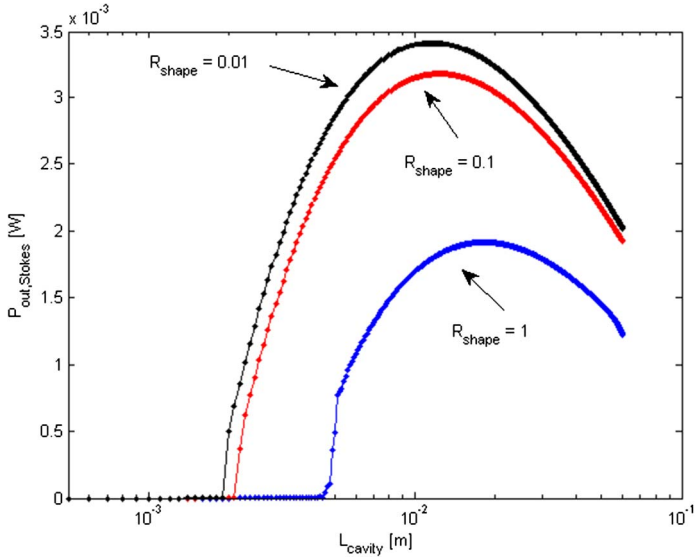

Fig. 23. Output power of the counter-propagating quasi-TE-polarized Stokes signal excited in the waveguide WG1, as a function of different cavity lengths and R_{shape}. The input pump power is constant, equal to 350 mW.

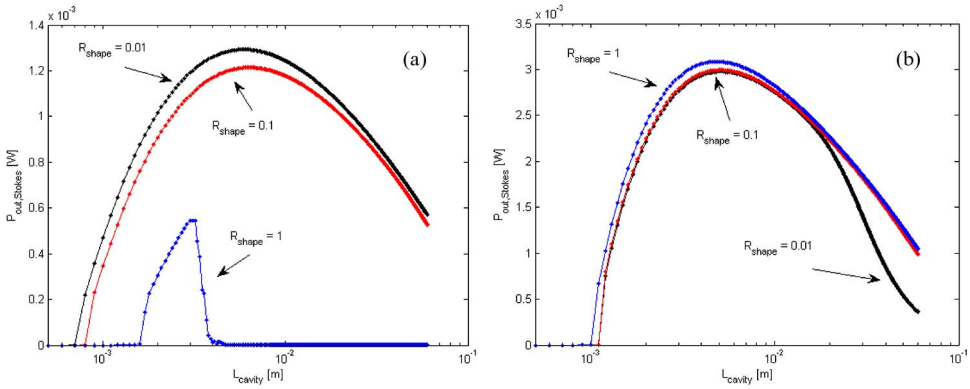

Fig. 24. Output power of the counter-propagating quasi-TE (a) and quasi-TM (b) polarized Stokes signal excited in the waveguide WG2, as a function of different cavity lengths and R_{shape}. The input pump power is constant, equal to 200 mW.

WG1 and WG2. In Fig. 23, the output power of the counter-propagating quasi-TE-polarized Stokes signal excited in the waveguide WG1 is shown as a function of different cavity lengths and R_{shape}. We can observe the optimal value of the resonant cavity length, since the curves present a maximum peak for each R_{shape} value in our simulations (i.e., 0.01, 0.1, and 1). In particular, by considering the waveguide configuration named WG1, it is convenient to refer to Fig. 11(b) too, where the normalized effective gains are plotted as a function of R_{shape} for various polarization state combinations. In fact, according to Fig. 11(b), the SRS gain in case of $p_{TE} \rightarrow s^{o}_{TE}$ emission tends to decrease with increasing R_{shape}. Consequently, by considering the same cavity length (e.g., $L_{cavity} = 1$ cm), the output Stokes power decreases with increasing the parameter R_{shape}. In addition, the presence of an optimal condition (curve peak) is justified because, by increasing more and more the cavity length, the SRS gain cannot compensate the propagation losses that the Stokes signal undergoes along multiple cavity roundtrips. Analogously, with decreasing more and more L_{cavity}, the Stokes signal excitation cannot occur when the pump signal propagates along a too short

distance. By considering the Raman laser based on WG1 with power coupling coefficients $\kappa^2_{p,TE} = 0.4$ and $\kappa^2_{s,TE} = 0.05$, the optimum cavity length of 1.16 cm results in case of $R_{shape} = 0.01$, while optimal values $L_{cavity} = 1.23$ cm and $L_{cavity} = 1.85$ cm are related to $R_{shape} = 0.1$ and $R_{shape} = 1$, respectively.

It is interesting to note, by the logarithmic scale in Fig. 22, the saturation and dropping down of the output Raman laser with increasing the input pump power, as induced mainly by TPA and FCA effects in case of quasi-TM (a) or quasi-TE backward Stokes wave (b). In Fig. 24(a) and (b), a similar analysis has been executed for the Raman laser based on WG2 with power coupling coefficient combinations $\kappa^2_{p,TE} = 0.4$, ($\kappa^2_{s,TE} = 0.05$, $\kappa^2_{s,TM} = 0.03$ - case (a)), and ($\kappa^2_{s,TE} = 0.02$, $\kappa^2_{s,TM} = 0.06$ - case (b)), assuming a pump power of 200 mW. As previously suggested for WG1, it is convenient to refer to Fig. 12(b) in case of $p_{TE} \rightarrow s^{\rho}_{TE}$ and $p_{TE} \rightarrow s^{\rho}_{TM}$ emissions. Analogous considerations discussed in the previous case can be extended to this case, too. In particular, for counter-propagating quasi-TE polarized Stokes signal, the trends of the curves plotted in Fig. 24(a) are similar to those already investigated in Fig. 23. Moreover, optimal cavity lengths are equal to 6 mm and 6.5 mm in case of $R_{shape} = 0.01$ and $R_{shape} = 0.1$, respectively, while a cavity length of 3 mm is suggested in case of $R_{shape} = 1$, although the output Stokes power is quite low (i.e., $\sim$0.6 mW). On the contrary, in case of counter-propagating quasi-TM polarized Stokes signal, as in Fig. 24(b), it is noteworthy to observe that any substantial difference cannot be appreciated among all three curves associated to R_{shape} values. This behavior is due because the SRS gain for $p_{TE} \rightarrow s^{\rho}_{TM}$ emission is characterized by a very smooth slope in the range extended from $R_{shape} = 0.01$ to $R_{shape} = 1$. Finally, a cavity length as long as 5 mm can be considered as optimal for all R_{shape} values considered in our investigation, with an output Stokes power as high as 3 mW. In conclusion, the Raman laser based on waveguide WG2 can be considered as the best design solution for simultaneously assuring high optical laser power, high external efficiency, relaxed fabrication tolerances, and compact dimensions. In particular, we obtain an output laser power of 3 mW for backward quasi-TM emission in 5 mm long cavity and an external efficiency of 21% (i.e., 4.2 %/mm), well larger than 10% in 3 cm long cavity (0.33 %/mm) demonstrated in Ref. [33].

4. Conclusion

The generalized model presented in this paper allows the wave evolution and power transfer (pump, Stokes) propagating in a SOI microcavity resonator to be accurately predicted, by taking into account the SRS and all other linear and non-linear physical effects involved in the Raman lasing mechanism. Analytical formulas have been derived in order to estimate the threshold power and the external efficiency for CW Raman laser based on a race-track resonator, resulting in a very useful tool for the design of such photonic devices. The influence of the waveguide sizes, pump and Stokes coupling factors, cavity shapes, polarization states, and waveguide orientations has been rigorously described and evaluated in order to select the fundamental design guidelines of integrated silicon Raman lasers. Finally, a number of numerical simulations are presented in order to estimate the Raman laser performance and confirm the physical predictions obtained from proposed design rules. Although not optimal, the designed laser structures have revealed external efficiencies and output powers well larger than those achieved in architectures presented in literature.

References

[1] J. Bowers, D. Liang, A. Fang, H. Park, R. Jones, and M. Paniccia, "Hybrid silicon lasers. The final frontier to integrated computing," *Opt. Photon. News*, vol. 21, no. 5, pp. 28–33, 2010.
[2] G. T. Reed, "The optical age of silicon," *Nature*, vol. 427, no. 6975, pp. 595–596, Feb. 2004.
[3] L. Pavesi, "Will silicon be the photonic material of the third millennium?" *J. Phys.: Condens. Matter*, vol. 15, no. 26, pp. R1169–R1196, 2003.
[4] M. N. Sysak, J. O. Anthes, J. E. Bowers, O. Raday, and R. Jones, "Integration of hybrid silicon laser and electroabsorption modulators," *Opt. Exp.*, vol. 16, no. 17, pp. 12478–12486, Aug. 2008.
[5] H. Park, A. Fang, D. Liang, Y. H. Kuo, H. H. Chang, B. R. Koch, H. W. Chen, M. N. Sysak, R. Jones, and J. E. Bowers, "Photonic integration on the hybrid silicon evanescent device platform," *Adv. Opt. Technol.*, vol. 2008, pp. 682978-1–682978-17, 2008.

[6] P. Mechet, F. Raineri, A. Bazin, Y. Halioua, T. Spuesens, T. J. Karle, P. Regreny, P. Monnier, D. Van Thourhout, I. Sagnes, R. Raj, G. Roelkens, and G. Morthier, "Uniformity of the lasing wavelength of heterogeneously integrated InP microdisk lasers on SOI," *Opt. Exp.*, vol. 21, no. 9, pp. 10622–10631, May 2013.
[7] L. Pavesi, L. D. Negro, G. Mazzoleni, G. Franzo, and S. Priolo, "Optical gain in silicon nanocrystals," *Nature*, vol. 408, pp. 440–444, Nov. 2000.
[8] J. Ruan, P. M. Fauchet, L. D. Negro, M. Cazzanelli, and L. Pavesi, "Stimulated emission in nanocrystalline silicon superlattices," *Appl. Phys. Lett.*, vol. 83, no. 26, pp. 5479–5481, Dec. 2003.
[9] M. Xie, Z. Yuan, B. Qian, and L. Pavesi, "Silicon nanocrystals to enable silicon photonics," *Chinese Opt. Lett.*, vol. 7, no. 4, pp. 319–324, Apr. 2009.
[10] A. Polman and F. C. J. M. Van Veggel, "Broadband sensitizers for erbium-doped planar optical amplifiers: Review," *J. Opt. Soc. Amer. B*, vol. 21, no. 5, pp. 871–892, May 2004.
[11] R. Claps, V. Raghunathan, O. Boyraz, P. Koonath, D. Dimitropoulos, and B. Jalali, "Raman amplification and lasing in SiGe waveguides," *Opt. Exp.*, vol. 13, no. 7, pp. 2459–2466, Apr. 2005.
[12] L. Sirleto, V. Raghunathan, A. Rossi, and B. Jalali, "Raman emission in porous silicon at 1.54 μm," *Electron. Lett.*, vol. 40, no. 19, pp. 1221–1222, Sep. 2004.
[13] O. Boyraz and B. Jalali, "Demonstration of a silicon Raman laser," *Opt. Exp.*, vol. 12, no. 21, pp. 5269–5273, Oct. 2004.
[14] M. Krause, H. Renner, and E. Brinkmeyer, "Analysis of Raman lasing characteristics in silicon-on-insulator waveguides," *Opt. Exp.*, vol. 12, no. 23, pp. 5703–5710, Nov. 2004.
[15] H. Rong, R. Jones, A. Liu, O. Cohen, D. Hak, A. Fang, and M. Paniccia, "A continuous-wave Raman silicon laser," *Nature*, vol. 433, pp. 725–728, Feb. 2005.
[16] H. Rong, A. Liu, R. Jones, O. Cohen, D. Hak, R. Nicolaescu, A. Fang, and M. Paniccia, "An all-silicon Raman laser," *Nature*, vol. 433, pp. 292–294, Jan. 2005.
[17] O. Boyraz and B. Jalali, "Demonstration of directly modulated silicon Raman laser," *Opt. Exp.*, vol. 13, no. 3, pp. 796–800, Feb. 2005.
[18] R. Claps, D. Dimitropoulos, and Y. Han, "Observation of Raman emission in silicon waveguides at 1.54 μm," *Opt. Exp.*, vol. 10, no. 22, pp. 1305–1313, Nov. 2002.
[19] R. Claps, D. Dimitropoulos, V. Raghunathan, Y. Han, and B. Jalali, "Observation of stimulated Raman amplification in silicon waveguides," *Opt. Exp.*, vol. 11, no. 15, pp. 1731–1739, Jul. 2003.
[20] A. Liu, H. Rong, M. Paniccia, O. Cohen, and D. Hak, "Net optical gain in a low loss silicon-on-insulator waveguide by stimulated Raman scattering," *Opt. Exp.*, vol. 12, no. 18, pp. 4261–4268, Sep. 2004.
[21] Q. Xu, V. R. Almeida, and M. Lipson, "Time-resolved study of Raman gain in highly confined silicon-on-insulator waveguides," *Opt. Exp.*, vol. 12, no. 19, pp. 4437–4442, Sep. 2004.
[22] Q. Xu, V. R. Almeida, and M. Lipson, "Demonstration of high Raman gain in a submicrometer-size silicon-on-insulator waveguide," *Opt. Lett.*, vol. 30, no. 1, pp. 35–37, Jan. 2005.
[23] R. L. Espinola, J. I. Dadap, Jr., R. M. Osgood, S. J. McNab, and Y. A. Vlasov, "Raman amplification in ultrasmall silicon-on-insulator wire waveguides," *Opt. Exp.*, vol. 12, no. 16, pp. 3713–3718, Aug. 2004.
[24] D. Dimitropoulos, V. Raghunathan, R. Claps, and B. Jalali, "Phase-matching and nonlinear optical processes in silicon waveguide," *Opt. Exp.*, vol. 12, no. 1, pp. 149–160, Jan. 2004.
[25] R. Claps, V. Raghunathan, D. Dimitropoulos, and B. Jalali, "Anti-Stokes Raman conversion in silicon waveguides," *Opt. Exp.*, vol. 11, no. 22, pp. 2862–2872, Nov. 2003.
[26] V. Raghunathan, R. Claps, D. Dimitropoulos, and B. Jalali, "Parametric Raman wavelength conversion in scaled silicon waveguides," *J. Lightw. Technol.*, vol. 23, no. 6, pp. 2094–2102, Jun. 2005.
[27] O. Boyraz, P. Koonath, V. Raghunathan, and B. Jalali, "All optical switching and continuum generation in silicon waveguides," *Opt. Exp.*, vol. 12, no. 17, pp. 4094–4102, Aug. 2004.
[28] R. Claps, V. Raghunathan, D. Dimitropoulos, and B. Jalali, "Influence of nonlinear absorption on Raman amplification in silicon waveguides," *Opt. Exp.*, vol. 12, no. 12, pp. 2774–2780, 2004.
[29] T. K. Liang and H. Ki Tsang, "Nonlinear absorption and Raman scattering in silicon-on-insulator optical waveguides," *IEEE J. Sel. Topics Quantum Electron.*, vol. 10, no. 5, pp. 1149–1153, Sep./Oct. 2004.
[30] R. Jones, A. Liu, H. Rong, M. Paniccia, O. Cohen, and D. Hak, "Lossless optical modulation in a silicon waveguide using stimulated Raman scattering," *Opt. Exp.*, vol. 13, no. 5, pp. 1716–1723, Mar. 2005.
[31] A. Liu, H. Rong, R. Jones, O. Cohen, D. Hak, and M. Paniccia, "Optical amplification and lasing by stimulated Raman scattering in silicon waveguides," *J. Lightw. Technol.*, vol. 24, no. 3, pp. 1440–1455, Mar. 2006.
[32] H. Rong, Y.-H. Kuo, S. Xu, A. Liu, R. Jones, M. Paniccia, O. Cohen, and O. Raday, "Monolithic integrated Raman silicon laser," *Opt. Exp.*, vol. 14, no. 15, pp. 6705–6712, Jul. 2006.
[33] H. Rong, Y.-H. Kuo, S. Xu, Y. Kuo, V. Sih, O. Cohen, O. Raday, and M. Paniccia, "Low-threshold continuous-wave Raman silicon laser," *Nature Photon.*, vol. 1, pp. 232–237, 2007.
[34] F. De Leonardis and V. M. N. Passaro, "Modeling of Raman amplification in silicon-on-insulator optical microcavities," *New J. Phys.*, vol. 9, no. 2, pp. 1–24, 2007, art. 25.
[35] M. Krause, H. Renner, S. Fathpour, B. Jalali, and E. Brinkmeyer, "Gain enhancement in cladding-pumped silicon Raman amplifiers," *IEEE J. Quantum Electron.*, vol. 44, no. 7, pp. 692–704, Jul. 2008.
[36] M. Krause, H. Renner, and E. Brinkmeyer, "Optical isolation in silicon waveguides based on nonreciprocal Raman amplification," *Electron. Lett.*, vol. 44, no. 11, pp. 691–693, May 2008.
[37] M. Krause, H. Renner, and E. Brinkmeyer, "Strong enhancement of Raman-induced nonreciprocity in silicon waveguides by alignment with the crystallographic axes," *Appl. Phys. Lett.*, vol. 95, no. 26, pp. 261111-1– 261111-3, Dec. 2009.
[38] N. Vermeulen, "Lasing directionality and polarization behaviour in continuous-wave ring Raman lasers based on micro- and nano-scale silicon waveguides," *J. Lightw. Technol.*, vol. 29, no. 14, pp. 2180–2190, 2011.
[39] *Comsol Multiphysics, ver.3.2, Single License*, COMSOL Inc., Stockholm, Sweden, 2005.
[40] V. M. N. Passaro and F. De Leonardis, "Space-time modeling of Raman pulses in silicon-on-insulator optical waveguides," *J. Lightw. Technol.*, vol. 24, no. 7, pp. 2920–2931, Jul. 2006.

[41] R. A. Soref and B. R. Bennett, "Electrooptical effects in silicon," *IEEE J. Quantum Electron.*, vol. QE-23, no. 1, pp. 123–129, Jan. 1987.
[42] F. De Leonardis and V. M. N. Passaro, "Modeling and performance of a guided-wave optical angular velocity sensor based on Raman effect in SOI," *J. Lightw. Technol.*, vol. 25, no. 9, pp. 2352–2366, Sep. 2007.
[43] H. Shin, W. Qiu, R. Jarecki, J. A. Cox, R. H. Olsson, A. Starbuck, Z. Wang, and P. T. Rakich, "Tailorable stimulated Brillouin scattering in nanoscale silicon waveguides," *Nature Commun.*, vol. 4, no. 1944, pp. 1–10, 2013.
[44] H. Rong, S. Xu, O. Cohen, O. Raday, M. Lee, V. Sih, and M. Paniccia, "A cascaded silicon Raman laser," *Nature Photon.*, vol. 2, pp. 170–174, 2008.
[45] V. M. N. Passaro and F. De Leonardis, "Investigation of SOI Raman lasers for mid-infrared gas sensing," *Sensors*, vol. 9, no. 10, pp. 7814–7836, 2009.
[46] D. Marcuse, "Computer model of an injection laser amplifier," *IEEE J. Quantum Electron.*, vol. 19, no. 1, pp. 63–73, Jan. 1983.
[47] A. Gajda, L. Zimmermann, J. Bruns, B. Tillack, and K. Petermann, "Design rules for p-i-n diode carriers sweeping in nano-rib waveguides on SOI," *Opt. Exp.*, vol. 19, no. 10, pp. 9915–9922, May 2011.
[48] M. Masi, R. Orobtchouk, G. Fan, J.-M. Fedeli, and L. Pavesi, "Towards a realistic modelling of ultra-compact racetrack resonators," *J. Lightw. Technol.*, vol. 28, no. 22, pp. 3233–3242, Nov. 2010.
[49] V. M. N. Passaro, F. Dell'Olio, C. Ciminelli, and M. N. Armenise, "Efficient chemical sensing by coupled slot SOI waveguides," *Sensors*, vol. 9, no. 2, pp. 1012–1032, 2009.
[50] V. M. N. Passaro, F. Dell'Olio, B. Timotijevic, G. Z. Mashanovich, and G. T. Reed, "Polarization-insensitive directional couplers based on SOI wire waveguides," *Open Opt. J.*, vol. 2, no. 1, pp. 6–9, 2008.
[51] *OptiBPM ver.7.0, Single License*, Optiwave Systems Inc., Ottawa, ON, Canada, 2005.